5-2008

# Real-Time Power Management of A Fuel Cell/ Ultracapacitor Hybrid

Wesley Greenwell
*Clemson University*, wgreenw@clemson.edu

# REAL-TIME POWER MANAGEMENT OF A FUEL CELL/ULTRACAPACITOR HYBRID

---

A Thesis
Presented to
the Graduate School of
Clemson University

---

In Partial Fulfillment
of the Requirements for the Degree
Master of Science
Mechanical Engineering

---

by
Wesley Douglas Greenwell
August 2008

---

Accepted by:
Dr. Ardalan Vahidi, Committee Chair
Dr. John Wagner
Dr. Randy Collins

# Abstract

This thesis presents the system architecture design, system integration methodology, and real-time control of a fuel cell/ultracapacitor hybrid power system. The main objective is for the hybrid system to respond to real-world fluctuations in power without negatively impacting fuel cell life.

A Proton Exchange Membrane (PEM) Fuel Cell is an electrochemical device which converts the chemical energy of pure hydrogen into electricity through a chemical reaction with oxygen. The high conversion efficiency, zero harmful emissions, high power-to-weight ratio, scalability, and low temperature operation make PEM fuel cells very attractive for stationary and portable power applications. However, fuel cells are limited in responding to fast transients in power demand, moreover power fluctuations have negative impact on fuel cell durability. This motivates the use of a supplementary energy storage device to assist the fuel cell by buffering sharp transients in power demand. The high power density, long cycle life, and efficiency of ultracapacitors make them an ideal solution for such auxiliary energy storage in a hybrid fuel cell system.

The power management strategy that determines the power split between the fuel cell and ultracapacitor is key to the power following capability, long-term performance, and life-time of the fuel cell. In this thesis, a rule-based and a model predictive control strategy are designed, implemented and evaluated for power management of a fuel cell/ultracapacitor hybrid. The high-level control objectives are to respond to rapid variations in load while minimizing damaging fluctuations in fuel cell current and maintaining ultracapacitor charge (or voltage) within allowable bounds.

An experimental test stand was created to evaluate the performance of the controllers. The test stand connects the fuel cell and ultracapacitor to an electronic load through two dc/dc converters, which provide two degrees of freedom, enabling independent low-level control of the DC BUS voltage and the current split between the fuel cell and ultracapacitor. Experiments show that both rule-based and model predictive power management strategies can be tuned to meet both high and low-level control objectives for a given power demand profile. However, the capability to explicitly enforce the constraints in model predictive scheme and its predictive nature in meeting power demands enables a more systematic design and results in general in smoother performance.

# Acknowledgments

I would like to express my gratitude to everyone on my advisory committee for their patience, understanding, and guidance throughout my graduate education here at Clemson University. A special thanks goes to my advisor, Dr. Ardalan Vahidi, for providing direction and focus throughout every step of my research and thesis preparation. He helped me break down what initially seemed like an impossible task into numerous simple solvable problems. His help with problem formulation, experimental methodology, controller development, conceptual understanding, and thesis organization/editing were crucial to my success. I would also like to thank Dr. John Wagner and Dr. Randy Collins for serving on my committee and providing assistance and advice on experimental setup and power electronics issues. Thanks also go to David Moline for his assistance with lab equipment and advice on a variety of technical topics.

I would like to thank those who provided assistance with compatibility issues between the hardware used in our setup and MATLAB® MPC Toolbox. Dr. Larry Ricker from the University of Washington and Dr. Alberto Bemporad from the University of Siena in Italy, authors of the MPC Toolbox, provided knowledge which was instrumental in the real-time implementation of MPC. A special thanks also goes to Rong Chen, a software developer from Mathworks, for his time and effort in solving hardware/software compatibility issues. The real-time implementation of model predictive control, a cornerstone of this work, would not have been possible without their gracious assistance.

# Table of Contents

# List of Tables

# List of Figures

# Chapter 1

# Introduction

A Proton Exchange Membrane Fuel Cell (PEMFC) is an energy conversion device which uses hydrogen and oxygen in a highly efficient electrochemical reaction to produce electricity with no harmful emissions. The high conversion efficiency, zero harmful emissions, high power-to-weight ratio, scalability, and low temperature operation make PEM fuel cells very attractive for stationary and portable power applications. However, due to limited response rate of its reactant supply subsystems, a PEMFC exhibits relatively poor dynamic performance, and is unable to follow sharp transients in power demand [6, 33, 58, 61, 66, 67, 68, 69]. Supplementing the fuel cell with an energy storage device which can buffer quick transients in power demand improves its load following capability. Also, the lifetime of the fuel cell stack is improved by reducing the large transients the stack must provide [19, 35, 58, 66, 68]. If an energy storage buffer is integrated in a fuel cell hybrid, the fuel cell can be sized to meet the expected power demand at steady-state [32, 68] and the energy storage device is sized to buffer the power transients.

Although batteries are the conventional choice for auxiliary energy storage, the ultracapacitor (UC) offers many advantages over batteries [16], especially in its ability to release large power in a short time. UCs provide the high power density of conventional capacitors with improved energy densities, resulting in an ideal storage device [28, 41]. They have been proven effective in reducing peak currents seen by the primary energy source in hybrid fuel cell systems [2, 38, 52, 70], resulting in increased fuel economy and extended stack lifetime. Unlike batteries which store and release energy through chemical reactions, UCs store energy electrostatically and have very low internal resistance. This results in very fast charge/discharge rates with very little power loss and overall charge/discharge efficiencies of greater than 95% [13]. Also in terms of lifetime UCs surpass even the most technologically advanced batteries. Some UCs have been reported as

having a lifetime of greater than 1 million full charge/discharge cycles, reducing the need for replacement or maintenance [10]. The low maintenance, long lifetime, high efficiency, and fast charge/discharge rates make UCs an ideal complement to the fuel cell in a hybridized power system [7, 38]. Moreover the energy density gap between batteries and ultracapacitors is decreasing every year thanks to advances in manufacturing and material technology [9, 14, 79].

A fuel cell/ultracapacitor (FC/UC) hybrid combines the high energy density of the hydrogen fuel cell with the high power density of the ultracapacitor (UC), resulting in a system with improved performance and potentially reduced size [26, 30, 33, 68, 71]. There are various hybrid system architectures for FC and UC integration and they vary in complexity and performance. A thorough discussion of system architectures including their advantages and disadvantages can be found in [22, 27, 56]. Different architectures differ in how the fuel cell and ultracapacitor are interconnected to the power BUS and in the power electronic devices used to control the BUS voltage and the power split between the fuel cell and ultracapacitor. Once the proper hybrid configuration and sizing is completed, it is this power split strategy in a FC/UC hybrid that plays a critical role in improved load-following, reduction of losses, and increased lifetime. In the literature a number of control methods has been proposed for meeting these objectives. Most of the existing work is tailored for power management of conventional hybrids with a combustion engine as the main propulsion unit. The control objective in most of the work is minimizing fuel usage. However similar ideas can be extended to power management of fuel cell hybrids.

Heuristic or rule-based control strategies are designed based on the engineer's experience or understanding of the system's components and interactions and their real-time control implementation is relatively simple. Many of the existing power management strategies use a rule-based supervisory controller at the high-level and simple filters [15, 31] or PID loops [6, 64, 67, 71] at low-level. Fuzzy-logic rule-based control schemes have also been used successfully for power management of hybrid electric vehicles [5, 24, 59, 62]. Other heuristic methods such as neural networks have also been proposed for power management [45, 51]. Although real-time implementation of these methods is relatively easy, they may not result in optimum trade-off between use of the power sources.

Dynamic programming (DP) techniques have been used to find the optimal power split offline [8, 54]. Lin et al. use deterministic dynamic programming for power management of a parallel hybrid truck [40]. Using this method, the optimal power split is determined offline by minimizing a penalty function. This process requires a priori knowledge of the drive cycle and cannot be performed in real-time, only rules extracted from the DP results can be used to make control decisions. In later studies, Lin et al. show

via simulations that deterministic DP can be outperformed by a stochastic dynamic programming approach [39], where the future control actions are based on probable drive cycles [60, 34]. Stochastic DP can be implemented in real-time, because it models future power demand as a stochastic process, but the results are sub-optimal.

Another promising control strategy, which does not require knowledge of the future drive cycle is the equivalent consumption minimization strategy (ECMS) [4, 29, 53, 58, 63]. This method determines optimal control actions based on a cost function quantifying the instantaneous cost of electrical and fuel energy. The key to successful implementation is determining the equivalence factor relating fuel and electrical energy. The method has resulted in improved performance and reduced fuel consumption in hybrid vehicles. In [46], Musardo et al. present an adaptive ECMS strategy where the electrical/fuel energy equivalence factor is estimated online according to driving conditions. Pisu and Rizzoni compare rule-based, A-ECMS, and H-infinity supervisory control strategies in [55], and determine that the A-ECMS strategy performs better than the other online-implementable methods..

In simulations, model predictive control (MPC) has been successfully used for power management of a FC/UC hybrid [72]. This optimal control method uses a linear model of the system to predict the response to future inputs and does not require a priori knowledge of drive cycle. A performance index is minimized to determine the power split which results in the optimal system performance. The main advantage of this approach is its ability to sense and avoid constraints during the operation of the hybrid system.

In this thesis, two control methods are presented for the power management of a FC/UC hybrid: 1) a rule-based strategy and 2) a model predictive control approach. The control objectives are to 1) minimize the current transients seen by the fuel cell, 2) follow the demand power as closely as possible, and 3) prevent over-charge/discharge of the ultracapacitor. The performance of both controllers are tested via simulation and experiments.

The thesis is organized as follows: Chapter 2 provides background information on the fuel cell-ultracapacitor hybrid system and its components. In Chapter 3, the setup of the hybrid test stand is discussed and testing procedures are explained. The control problem is formulated and the real-time implementation of the control strategy is explained in Chapter 4. In Chapter 5, the simulation and experimental results are discussed. Finally, in Chapter 6, conclusions are drawn based on the controller/system performance in meeting its objectives.

# Chapter 2

# Fuel Cell/Ultracapacitor Hybrid and Its Components

This chapter provides general background material necessary for understanding the operation and control of hybrid power systems in general and fuel cell-ultracapacitor hybrids in particular. The current technology, principles of operation, and performance characteristics of both fuel cells and ultracapacitors are discussed. Finally, a discussion on power electronics provides details on the integration of the various components of a hybrid system.

## 2.1 Fuel Cells

In a fuel cell electricity is harnessed from the oxidation/reduction reaction occurring between a gaseous fuel and oxidant introduced at the anode and cathode, respectively. This process of converting electrochemical potential energy into electricity is similar to the process occurring in a galvanic cell, or battery. However, unlike the battery, the fuel cell's energy production is not limited by constantly depleting electrodes. In theory, as long as the balance of reactant supply and byproduct removal is maintained, a fuel cell can generate electricity indefinitely. There are many different reactants that can be used in different types of fuel cells.

### 2.1.1 Fuel Cell Types

Fuel cells are commonly classified based on the electrolyte used in their chemical reaction. Each type of fuel cell may require specific fuels and catalysts, depending on the chemical reaction they employ. The different types of fuel cells therefore differ in their operating temperatures, byproducts, and overall efficiency. These differences in general operation determine what type fuel cells are used for different applications. The five most common types of fuel cell are:

- Solid Oxide Fuel Cell (SOFC)
- Molten Carbonate Fuel Cell (MCFC)
- Phosphoric Acid Fuel Cell (PAFC)
- Alkaline Fuel Cell (AFC)
- Proton Exchange Membrane Fuel Cell (PEMFC)

Due to its high power to weight ratio, low operating temperature, and quick start time, the proton exchange membrane (PEM) fuel cell, sometimes referred to as the polymer electrolyte membrane fuel cell, is the most commonly used fuel cell for portable power applications. As a result, any mention of fuel cells in the remainder of this thesis is referring to the PEM fuel cell.

### 2.1.2 Principles of Fuel Cell Operation

The PEM fuel cell is a type of hydrogen fuel cell. It is an energy conversion device which uses gaseous hydrogen as a fuel and oxygen as an oxidant. The fuel cell's only emissions are water and heat.

#### Fuel Cell Construction

A single PEM fuel cell consists of two main components: the flow field plates and the membrane electrode assembly (MEA). As shown in Fig. 2.1, each individual cell contains an MEA sandwiched by two flow field plates which act together to promote the electrochemical reaction and the generation of electricity. Gas diffusion plates disperse the hydrogen and oxygen evenly over the surface of the anode and cathode where the reactions take place. The voltage generated in a cell is directly proportional to the surface area on which these reactions occur, therefore careful design and construction of the plates is required to ensure proper circulation and dispersion of the reactants.

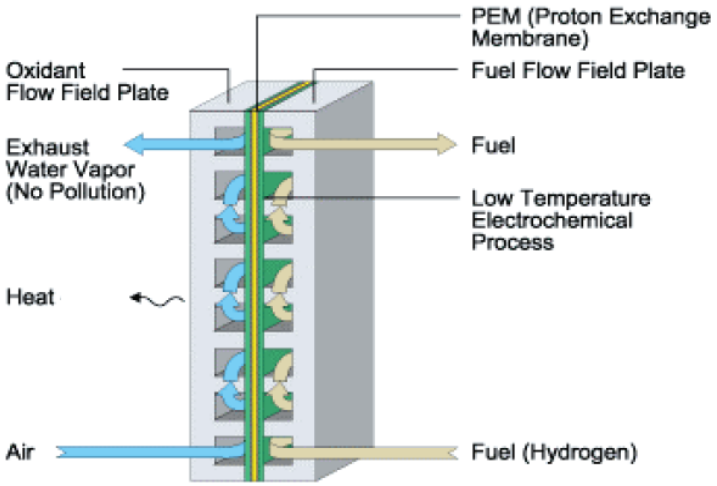


Figure 2.1: Membrane Electrode Assembly [3].

The reactants are transported through the flow field plates to the membrane electrode assembly where the chemical reactions take place and electricity is harnessed. The MEA consists of the proton exchange membrane, anode, and cathode. The PEM is a thin, ion-conducting membrane which allows only protons to pass from the anode to the cathode side of the cell. This membrane is sandwiched on each side by the anode and cathode, which are thin, porous carbon sheets coated with a platinum catalyst. The platinum catalyst promotes the oxidation and reduction reactions occurring in the anode and cathode, respectively. The porous anode and cathode allow the transfer of protons through the membrane and provide maximum surface area on which the chemical reactions can occur.

**Electrochemical Reaction**

The chemical reaction that occurs in the hydrogen fuel cell is an oxidation/reduction reaction. Hydrogen is oxidized in the anode and oxygen is reduced in the cathode. The resultant products combine after the electrical energy has been harvested and create water and heat, the only byproducts of the process.

As the flow field plates deliver pressurized gaseous hydrogen to the anode side of the MEA, the platinum catalyst helps oxidation of the hydrogen molecules. Oxidation is the loss of electrons, or an increase in charge. Oxidation of a hydrogen atom produces a hydrogen ion (proton) and an electron. For a single

hydrogen molecule, the result is:

$$H_2 \Longrightarrow 2H^+ + 2e^- \tag{2.1}$$

The hydrogen ions, or protons, pass through the PEM to the cathode side of the MEA. The leftover electrons built up in the anode, resulting in a charge imbalance, or electric potential between the anode and cathode. By connecting an external load circuit between the anode and cathode, electricity is harnessed as electrons flow due to the cell voltage difference.

On the cathode side of the fuel cell, pure oxygen or air is pumped in. The oxygen, electrons, and hydrogen ions meet in the presence of a platinum catalyst and undergo a reduction reaction to produce water.

$$\frac{1}{2}O_2 + 2e^- + 2H^+ \Longrightarrow H_2O \tag{2.2}$$

The half-reactions occurring in the anode and cathode can be expressed as a total fuel cell reaction given by Equation 2.3. The resulting PEM fuel cell reaction uses hydrogen fuel and oxygen to create electricity with the only byproducts being heat and water.

$$H_2 + \frac{1}{2}O_2 \Longrightarrow H_2O \tag{2.3}$$

### 2.1.3 Fuel Cell System and Auxiliary Components

A single fuel cell doesn't produce enough power for many applications, so individual fuel cells are stacked together to be able to provide increased electrical power. Fuel cells can be stacked in series to increase voltage and stacks can be placed in parallel to increase current capacity for a given application. A fuel cell system is a combination of these fuel cell stacks along with all auxiliary subsystems and components, which are required for the stacks to operate properly. Appropriate sizing of each of these components is crucial to ensuring a long stack lifetime and proper performance. Some of the most important auxiliary components, and their purposes, are discussed next.

#### Reactant Delivery and Storage

The reactants required for operation of the fuel cell must be delivered to each electrode in concentration levels that ensure completion of the chemical reactions. Failure to maintain these reactant ratios

during fuel cell operation is referred to as stack "starvation" and can cause permanent damage to the polymer electrolyte membrane.

Pressure regulators are required to maintain the hydrogen pressure inside the stack at a desirable level. It is important that the hydrogen be pure, contaminant-free gas. In reality, the hydrogen is never 100% pure and contaminants which don't react will build up in the anode side of the fuel cell during normal operation. A purge valve is common in fuel cells in order to purge at regular intervals these contaminants as well as excess water build-up.

Pure hydrogen gas can be compressed and stored in tanks, but the resulting gas has low volumetric energy density, or energy content per unit volume. This means that large storage tanks are required for extended fuel cell operation. These tanks are not the most practical, especially for portable applications such as electric vehicles. The hydrogen can be stored as liquid hydrogen for increased volumetric energy density. Cryogenic temperatures are required for liquid hydrogen storage, necessitating additional equipment and energy, thus reducing system efficiency. The hydrogen can also be stored in metal hydrides or hydrocarbon fuels, such as methanol. Metal hydride storage is an emerging technology and will require advancements before it is a viable option. On-board reformers are required to release hydrogen from hydrocarbon fuels. These reformers result in increased size, decreased efficiency, and production of harmful gases negating the attractive "no emission" production of electricity from the fuel cell.

In order to complete the reaction, the cathode needs to be supplied with oxygen. Pure oxygen supplied to the cathode ensures the most efficient operation of the fuel cell. This oxygen can be stored in tanks, but this results in limited supply issues and extra system size. PEM fuel cells commonly use an air compressor or a blower to supply oxygen to the cathode.

**Stack Humidity and Temperature Control**

Stack humidity and temperature must be regulated at all times to ensure proper operation [35, 65]. In an air-cooled fuel cell, a cooling fan is also used to regulate the stack temperature within an acceptable range. Larger fuel cells may be water-cooled.

The humidity in a fuel cell stack must also be carefully regulated. Fuel cell systems generally have an integrated humidifier to ensure that the humidity inside the fuel cell stack is at desirable levels. If the humidity is too low, the polymer electrolyte membrane may dry out. Water is necessary for the hydrogen ions to permeate the membrane, thus the membrane must be saturated to ensure high ionic conductivity of the electrolyte. A dry membrane is also more prone to cracking and tearing. If the humidity is too high, then

excess water can condense in the cell, blocking possible reaction sites and reducing stack efficiency. Lee et al. performed simple tests to show the dramatic performance decrease from a fuel cell stack with improper humidification [37].

#### Fuel Cell Controller

A fuel cell system needs a supervisory controller to ensure the fuel cell stack and all the auxiliary components work together to generate electricity without harming the fuel cell. The controller must monitor parameters such as stack current, cell voltages, water build-up, reactant concentrations, stack pressures, stack temperature, and stack humidity. The controller must then determine and apply the proper control actions to the air compressor, cooling fan, pressure regulator, purge valve, etc. A properly operating controller is crucial to long-term performance of the fuel cell system.

### 2.1.4 Performance Characteristics

Although expensive catalysts are used to enable the chemical reactions and improve the dynamic response, the fuel cell has inherently slower dynamics when compared to various other energy sources. Not only does the fuel cell respond slowly to sharp transients in demand, but these transients can cause stack degradation and decreased efficiency. Various operational/performance characteristics of the fuel cell are discussed below as well as their implications on a power system.

#### Fuel Cell System Efficiency

An important performance measure of any power source is its efficiency. The fuel cell efficiency is the ratio of the amount of electrical energy harnessed from the cell over the energy content of hydrogen. Unlike an internal combustion engine (ICE), which uses combustion of fuel to create heat and then mechanical work, a fuel cell converts energy directly from chemical bonds to electrical energy. This is a relatively efficient process with little heat loss resulting in a theoretical cell efficiency of 83% [23], and practical cell efficiencies around 70% [75].

For a fuel cell stack, other losses include cell losses, line resistance losses, and power losses from running auxiliary pumps, fans, etc. Practical efficiencies of large industrial fuel cell systems range from 60% at no load to 40% at full load [23].

Experimental data was retrieved from a Nexa$^{TM}$ PEM fuel cell in our lab at Clemson to determine

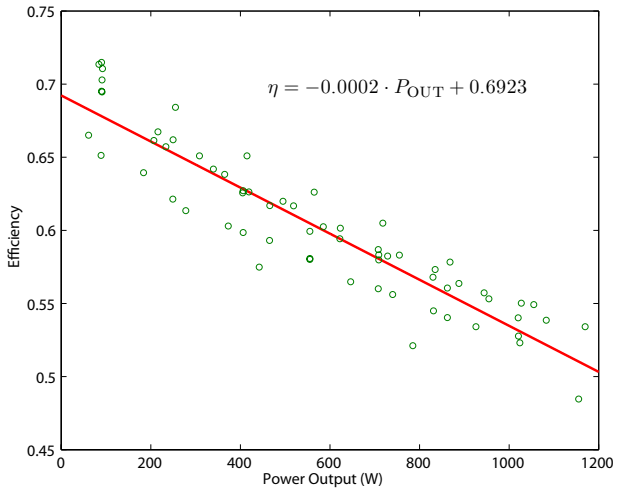


Figure 2.2: Nexa$^{\mathrm{TM}}$ Efficiency vs. Power Output Based on Experiments Performed at Clemson.

its efficiency in relation to the power it is providing. The fuel cell was stepped through various power levels, and the fuel flow-rate required to maintain that power output was determined. The overall system efficiency was calculated as the power output (as sensed from the output terminals) over the theoretical power, which is determined from the hydrogen fuel flow-rate and energy content (higher heating value). The system efficiency calculation is shown in Eq. 2.4. Note that $Q_H$ is the volumetric flow-rate and $U_H$ is the energy density of hydrogen gas.

$$\eta = \frac{P_{OUT}}{P_{THEORY}} = \frac{P_{OUT}}{Q_H \cdot U_H} \tag{2.4}$$

The plot of the fuel cell efficiency versus output power is shown in Fig. 2.2. The fuel cell system efficiency seems to be inversely proportional to the power it is supplying. For the Nexa$^{\mathrm{TM}}$ fuel cell, the efficiency varies from around 70% at no load to 50% at maximum load (1200 $W$). It should be noted that these efficiency values were determined from the fuel consumption steady state, or after the fuel cell module had settled after a step in loading. The efficiencies during transients are lower, another motivating reason to maintain steady fuel cell current. An extensive study by Choi et al. shows that ripple current in the fuel cell (which occur during sharp load transients) cause a 10% reduction in output power [17].

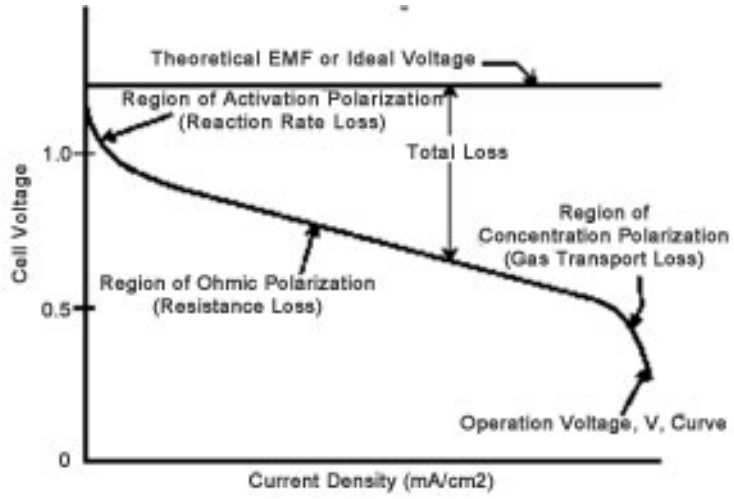


Figure 2.3: Fuel Cell Polarization Curve (Provided by AMETEK, Inc.[57]).

**Fuel Cell Polarization/Performance Losses**

The electrochemical reaction occurring in a hydrogen fuel cell can be used to determine the theoretical, or ideal voltage of an individual cell. The voltage generated is based on the oxidation potential of hydrogen, or its potential for releasing electrons and the *Gibbs free energy* for the reaction. Details on this calculation can be found in various texts [3, 23]. When the cell input is gaseous hydrogen, the maximum theoretical cell voltage is 1.18 $V$ [57]. The actual cell voltage can be directly related to the cell's efficiency. Any drop from this theoretical cell voltage implies internal losses and reduced efficiency.

Internal losses in PEM fuel cells can be lumped into three main categories: activation, resistance, and gas transport losses. The total cell loss is the sum of each of these three system losses. The regions in which these losses occur can be seen in the fuel cell polarization curve shown in Fig. 2.3. This plot relates an individual cell voltage to the current density drawn. The current density is the current delivered divided by the effective area of the cell.

Activation polarization losses, or losses due to slow electrochemical reaction rates, occur at relatively low current densities. This sharp decrease in cell voltage is due to the fact that the at low current draw, the energy available to initiate the chemical reactions at the catalyst surface is low. Therefore, a reduction in the flow of electrons results in a decrease in electric potential.

Resistance polarization, otherwise known as ohmic polarization, occurs over a wide portion of the fuel cell operating range. These losses are due to resistance to electron conduction in the electrodes and to

ionic conduction in the electrolyte and proton exchange membrane. These losses obey Ohm's law and are proportional to the current drawn from the stack.

The last major type of fuel cell polarization loss occurs at very high current draw. These losses are due to bottlenecks in reactant/product transport and are referred to as concentration losses or gas transport losses. In this case, the flow field plates and hydrogen supply are unable to provide the reactants as fast as they are being consumed and the rate of water production exceeds the removal rate. The resulting lack of reactants and surface area on which they can react leads to a large drop in voltage.

## 2.2 Ultracapacitors

Ultracapacitors (UCs), sometimes referred to as supercapacitors or electrochemical double layer capacitors (EDLC), are devices which can store energy electrostatically. These devices are analogous, in both operation and performance, to conventional capacitors which are commonly used for filtering and load-leveling small electronic circuits. The main difference is that UCs are high-capacity versions of these conventional capacitors, and thus have the capability to serve similar purposes on a larger scale. One application of UCs is energy storage in hybrid power systems, such as electric vehicles. If properly utilized, they help reduce fuel consumption, improve load following capabilities, and decrease stresses placed on other components in the system. The main limitations to the widespread use of UCs in portable power systems has been their relatively low energy densities (compared to advanced batteries); but recent advances in the materials and their manufacturing technologies is helping increase energy density of UCs. In order to understand how this increased energy storage is possible in UCs, it is important to understand the basics of capacitance, which is the topic of the next section.

### 2.2.1 Capacitance and Energy Storage

Capacitors are electronic devices which use charge separation, or electric fields to store electrical energy. Conventional dielectric capacitors consist of two parallel conducting plates separated by an insulator, or dielectric. When a voltage is applied across the capacitor plates, or terminals, the plates become oppositely charged. The plate connected to the negative terminal of the voltage source accepts electrons and becomes negatively charged while the plate connected to the positive terminal of the voltage source loses electrons, becoming positively charged. The electrons flow in this manner until the voltage across the capacitor equals the source voltage. At this point, the repelling forces at the electrodes equal the force due to the applied

potential. The dielectric insulator prevents the transfer of electrons between the two electrodes, resulting in charge separation and an electric field. In the presence of this electric field, the dielectric becomes polarized, meaning its ions align themselves with the field created by the two plates. The voltage sources can be removed and the capacitor will stay charged until an external circuit uses the stored energy.

A measure of the amount of charge a capacitor can store for a given voltage is referred to as its capacitance and has the unit of Farads (coulombs/volt). By increasing the size of the electrodes and moving the plates closer together, the electric field becomes stronger, resulting in higher capacitance and more energy storage. The capacitance also depends on the absolute permittivity, $\varepsilon$, of the dielectric material (also known as the dielectric constant). This is measure of the dielectric insulator ability to polarize in the presence of an electric potential or field. The relationship between these properties is shown in Eq. 2.5.

$$C = \varepsilon \frac{A}{d} \tag{2.5}$$

Another important property of the dielectric material is its dielectric strength, or ability to withstand large voltages. This value depends on the thickness of the dielectric and determines the rated voltage of the capacitor. If a capacitor is operated above its rated voltage, the dielectric can break down and begin to conduct electrons, creating an electrical short circuit.

### 2.2.2 Principles of Ultracapacitor Operation

The downside to conventional capacitors is that their capacitances are in the microfarad range, meaning they provide very small amount of charge storage. These energy storage devices are convenient for small electronic devices, but it is often desirable to have larger energy storage for larger applications. Ultracapacitors use electrodes with extremely high surface area separated by very small distances resulting in capacitance values several orders of magnitude greater than conventional capacitors. The construction is slightly different and is made possible by improvements in advanced materials and micro-manufacturing.

A single ultracapacitor consists of two electrodes, an electrolyte, and a thin separator membrane as shown in Fig. 2.4. Current collectors are often included to reduce ohmic losses and provide a solid conductive path from the electrodes. The two conductive electrodes are submersed in the electrolyte solution. When a voltage in imparted on the two plates, the negative electrode collects electrons and the positive electrode releases electrons. The ionization of the electrolyte occurs when the voltage is applied at the electrodes and the anions and cations within the solution accumulate near the positive and negative electrodes, respectively.

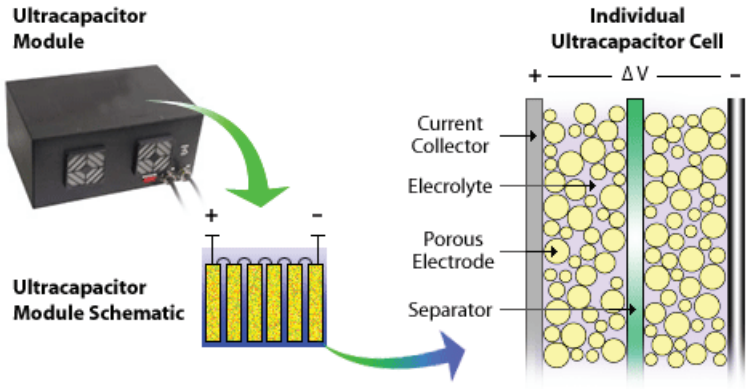


Figure 2.4: Ultracapacitor Construction (Provided by Ultracapacitors.org.[1]).

The nature of the electrode/electrolyte interface prevents ion transfer between the two, resulting in a build-up of two layers of charges at this interface. These layers present at the positive and negative terminal of the UC are referred to as the "electric double layer". The separation of charges in this double layer can be as small as $0.3-0.5\ nm$ [18], resulting in extremely large energy storage capabilities. The separator membrane prevents the short circuiting of the UC by providing electrical insulation while allowing ions to pass.

The capacitance of these devices is directly proportional to the electrode surface area. The electrodes are most commonly made from activated charcoal, or carbon. These highly porous, sponge-like carbon sheets maximize conductor surface area for a sheet size. Current technologies are allowing the manufacture of carbon electrodes with specific areas as high as $2000\ m^2/g$ [41, 79]. TDA Research, Inc. has determined through extensive research, that current electrodes are allowing measured capacitances on the range of $20-40\%$ of what is theoretically possible, leaving room for improvement [20, 21]. Numerous other research efforts in the development of new electrode materials with extremely high specific areas are currently underway.

Ultracapacitor assembly involves producing large multi-layer sheets with electrodes sandwiching a separator. The compound sheets are wound to reduce size, placed in packaging, and filled with an electrolyte. The electrolytic solution and separator membrane create the very small gap between the electrodes. Due to the extremely small charge separation distance, UCs currently have a breakdown voltage of $2.67\ V$ [42, 50, 76]. Therefore, UCs are generally purchased as modules consisting of several cells stacked in series and parallel to increase the voltage and energy storage for a specific application. They are generally purchased as completely encased modules with integrated cell monitoring/balancing electronics to ensure voltage balance between each cell.

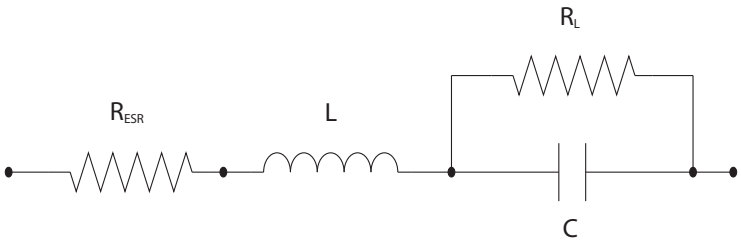


Figure 2.5: Lumped Ultracapacitor Electrical Model

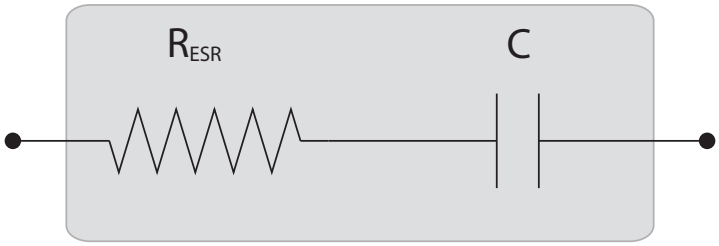


Figure 2.6: Simplified Ultracapacitor Electrical Model

### 2.2.3 Ultracapacitor Modeling and Performance Characteristics

A common electrical circuit model of a UC bank can be seen in Fig. 2.5. In this model, the UC is lumped into four elements. The UC capacitance is denoted by $C$ and is connected in parallel with the leakage resistance, $R_L$. The equivalent series resistance $R_{ESR}$ and equivalent series inductance $L$ are then connected in series.

The leakage resistance represents the UCs losses due to self-discharge. This type of discharge is generally very small and could be attributed to an electrolyte solution with a small leakage current or internal short circuiting. In many cases, the leakage resistance $R_L$ can be neglected. The inductance arises naturally in the construction of the module but can generally be neglected, especially in DC power applications such as the one considered here. The ESR is the combination of all internal resistance in the module leading to power losses according to Ohm's law. The equivalent series resistance (ESR) cannot be neglected in general. For the application considered here, a simplified model is used, consisting of a capacitor and a resistor connected in series as shown in Fig. 2.6. Although the UCs ESR and capacitance are dependent on its internal temperature, the dependency is so slight that its effects are negligible [36].

The governing equations for this simple UC model are the same as the governing equations for a

conventional capacitor. The amount of charge (in coulombs) stored in the capacitor is proportional to the potential across its terminals. The relationship between voltage, capacitance, and charge is given in Eq. 2.6.

$$Q = CV \tag{2.6}$$

By taking the time derivative of the capacitor charge, the relationship between UC current and voltage can be determined and is given in Eq. 2.7. The current flowing into or out of the UC in amps (C/s) is related to the rate of change of UC voltage.

$$I = \frac{dQ}{dt} = C\frac{dV}{dt} \tag{2.7}$$

The UCs instantaneous power is the product of the current and voltage. Taking the integral of the power gives the relationship between capacitor voltage and energy stored. The total energy storage can be found by integrating this relationship from 0 $V$ to some voltage $V$, as shown in Eq. 2.8. Note that the amount of energy storage is proportional to the UC voltage squared. This means that by depleting the UC from full charge to half charge uses 75% of the total energy stored.

$$p = VI = CV\frac{dV}{dt} \quad \Rightarrow \quad E = \int_0^t p\,dt = \int_0^V CV\,dV = \frac{1}{2}CV^2 \tag{2.8}$$

The energy storage of a UC bank is often expressed in watt-hours (Wh), or the amount of constant power that the UC could deliver over an hour. A normalized measure known as the energy density (Wh/kg) is frequently used to relate the energy storage to the mass of the UC module. UC modules currently available can provide energy densities of $0.5 - 10\ Wh/kg$ [76]. The normalized measure relating power to mass is the power density (W/kg), and UC modules can provide power densities of $2000 - 4000\ W/kg$ [44, 11].

### 2.2.4 Ultracapacitor vs. Battery

Ultracapacitors are becoming a popular alternative to batteries in applications which require portable high power delivery. UCs are ideal for pulsed load applications, where large transients in power demand are most efficiently met by a high power density device. The bank acts as an energy buffer or load-leveling device to reduce stress on other system power sources and increase load-following performance capabilities. In portable power applications, such as the electric vehicle, batteries are currently more popular than UCs because they are capable of storing larger energy densities. Improvements in UC technology, leading to high-

end modules with capacitances as high as 5000 $F$ [50, 79], are making UCs more viable for use in portable power applications [16].

Electrochemical batteries store charge in chemical form. This chemical process is very slow resulting in low power densities compared to UCs. Over time, the electrodes in a battery, which chemically react to release energy, are depleted and impurities in the cell lead to chemical deposits. Attempting to draw current from the cell at high rates results in further battery degradation. All this results in significantly decreased battery performance and lifetime.

Unlike batteries which require a chemical reaction to provide power, UCs store energy in an electric field. There are many benefits to this method of storing energy. The polarization of the electrolyte is a highly reversible process resulting in very high cycle life. UCs can be charged and discharged through many cycles with little degradation to the operation of the device. This extended cycle life is one of the main advantages of using the UCs in electric vehicles.

Through careful manufacturing and the use of high-quality, high-conductivity materials, the ESR on high-end capacitors can be as low as 0.33 $m\Omega$ [50]. The low resistance allows the UC to provide currents exceeding 5000 amps [43] and extremely large power densities when compared to batteries. Of course, power losses are proportional to the UC bank current, so increased current levels result in a decrease in module efficiencies [11]. Even at large charge/discharge rates, UC modules can provide extremely high round-trip efficiencies ranging from $90-95\%$ [12]. Efficiencies as high as 95% have been achieved in UCs with discharge power densities of $1200W/kg$ [11].

The ability to absorb high power makes UCs ideal for regenerative braking of electric vehicles [52, 74]. Whereas UCs can be charged and discharged in seconds, batteries can take minutes or even hours to safely charge and discharge. A fast charge time (0 to full charge) on standard Ni-MH battery is considered to be about $0.25-1.5$ hours [47]. Since braking an electric vehicle is a quick process absorbing a lot of energy, using batteries to absorb this energy can significantly decrease their lifetime. In a comparative study, UCs high charge/discharge rates result in a $10-15\%$ improvement in fuel economy when compared to advanced batteries [12].

From a practical implementation standpoint, the UCs low ESR results in very little resistance heating even at high currents, meaning the UCs maintain reasonable temperature. The UC modules have no moving parts which means better reliability and very low maintenance. They can be installed in any orientation, have a long shelf-life, and are available in a variety of dimensions. Another benefit of UCs is that their stored charge is easy to monitor since it is directly related to voltage, unlike the battery which has highly nonlinear

SOC/voltage relationship. Unlike batteries, which must be replaced frequently, the virtually unlimited life cycle of UC modules make them a more environmentally friendly and more economical [51] option in the long run. All these benefits makes ultracapacitors competitive with batteries for energy storage in hybrid power systems.

## 2.3 Fuel Cell-Ultracapacitor Hybrid

In a hybrid power system the load receives power from more than one source. There are many local and global system benefits of using several power supply devices in a coordinated, hybrid system. Several key concepts in hybrid power sources, with a focus on the FC/UC hybrid, are discussed in the following sections.

### 2.3.1 Hybrid Configurations

There are many ways these hybrid systems can arrange their energy supply and storage devices. The choice between these various hybrid architectures, each of which have their own advantages and disadvantages, is highly dependent on the application. Some common architectures are discussed here for an application using a hydrogen fuel cell and UC bank. The load is a simple energy sink and can simulate an electric motor for example. Power electronics are used for interconnection and control of the power sources. Further information on hybrid system architectures can be found in the references [22, 27, 56].

The simplest hybrid configuration is shown in Fig. 2.7. In this configuration, the fuel cell and UC bank are connected in parallel directly to the bus. This method of connection utilizes no DC/DC converters, therefore the size, weight, and cost of the hybrid system are greatly reduced. Fewer components also means system reliability is improved because there are fewer devices that can potentially fail. The downside to this simple configuration is that the load draws power from the combined system at the BUS voltage determined by the fuel cell and UC bank dynamics. This method does not allow active control over the BUS voltage or current distribution between the two sources, and is therefore impractical for most applications.

The addition of a power electronic converter to the hybrid architecture as shown in Fig. 2.8 allows more control over the operation of the system. Many applications require that the load receive power at a constant BUS voltage. Since the fuel cell and UC bank voltage are unregulated, at least one DC/DC converter must be included to ensure a constant bus voltage.

Figure 2.9 shows some hybrid system architectures which utilize two DC/DC converters. By adding an extra degree of freedom, two converters greatly improve the controllability of the hybrid system, but add

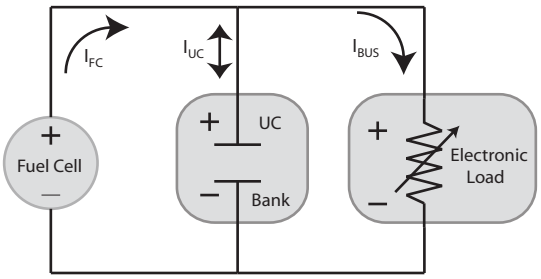


Figure 2.7: Hybrid System Architecture with No Power Electronics.

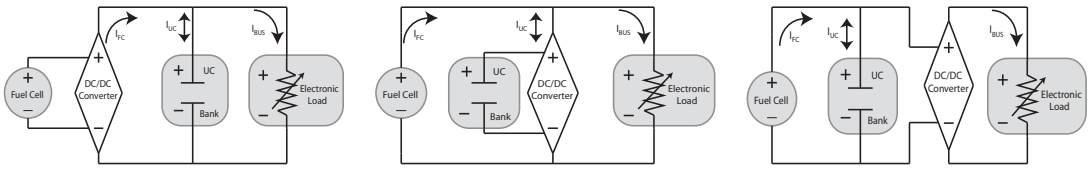


(a) FC Converter (b) UC Converter (c) BUS Converter

Figure 2.8: Hybrid System Architecture with Single DC/DC Converter.

size, weight, and cost. Because the system has two sources, at least two converters are required to completely control the bus voltage and power split between the two sources. In many cases, the benefits of having that extra control may outweigh the losses associated with adding another converter.

The advantages of an actively controlled UC bank through DC-DC converter are discussed in relation to a passive connection in a battery/UC hybrid [25]. Some of the advantages include: 1) the UC voltage can be different than the other energy source, 2) the peak power capacity is increased, 3) variations in load voltage are reduced, and 4) system size and weight can be decreased. However, the total system losses are in-

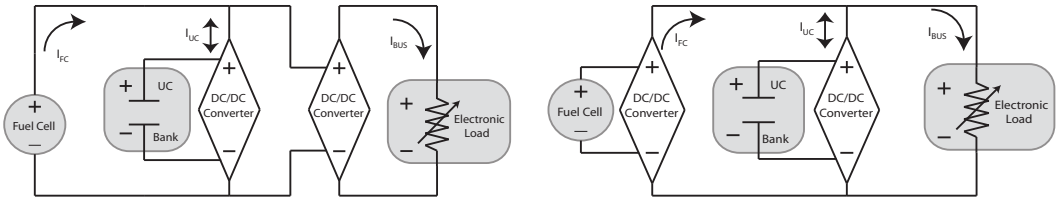


(a) UC and BUS Converter (b) UC and FC Converter

Figure 2.9: Hybrid System Architecture with Two DC/DC Converters.

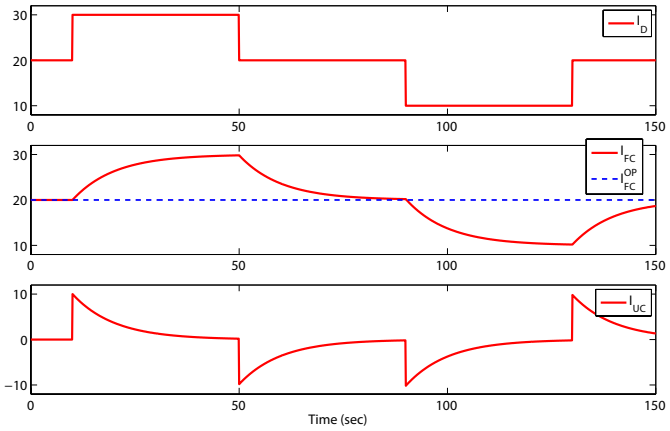


Figure 2.10: Ideal FC/UC Hybrid Performance Under Load Transients.

creased by the addition of the converter and the high current operation of the UC bank. In this case, converter losses account for 50% of the total losses in the hybrid power system [25].

Ultimately, the decision on what type of hybrid system configuration to use depends on the limitations and requirements of the application. The application considered in this thesis, requires both precise control of power split and a constant voltage bus. The architecture chosen for use in this case is shown in Fig. 2.9b where the fuel cell and UC bank each have their own converter and are connected in parallel to the BUS. The fuel cell converter is used to maintain the BUS voltage and the UC converter is used to implement current control.

### 2.3.2 Integrated Operation

Fuel cells can provide steady power for long periods of time (high energy density); UCs can provide short bursts of high power (high power density). By exploiting the advantages of each source's operation in a properly controlled hybrid system, improved system and component performance can be achieved. The control of a such a system can be broken down into system objectives (high-level) and subsystem objectives/constraints (low-level). The system objectives include meeting power demand and reducing fuel consumption. The subsystem objectives are to keep the SOC of the UC in a desired range and reduce transients seen by the fuel cell. The control goal is to meet the high-level objectives without violating low-level constraints.

Figure 2.10 shows the ideal response of the fuel cell/ultracapacitor hybrid to a transient in current demand (assume constant voltage BUS). Initially, the hybrid is in steady state and the fuel cell is providing

the full current demand. Upon sudden change of the current demand, instead of the fuel cell providing the desired current, the high power UC buffers the steps. This allows a smoother transition of fuel cell current which is favorable to fuel cell durability. The two sources work together to meet the demand (high-level) without violating subsystem constraints (low-level). In some cases, the UC may approach a SOC violation, at which point more complex control actions must be taken for optimal control of the system. DC/DC converters are used to accomplish this system control and are considered in the next section.

## 2.4 Power Electronics

The control, conversion, and conditioning of electrical power in hybrid systems is achieved by power electronic devices. These devices can be classified according to their input/output forms as follows: AC to DC (rectification), DC to AC (inversion), DC to DC (conversion), and AC to AC (conversion). Since this application is concerned with conversion from DC sources to a DC load, DC/DC converters are the only power electronic devices discussed in this thesis.

### 2.4.1 Linear Regulators vs. Switched-Mode Converters

Before advances in semiconductor technology made switched-mode converters possible, the power electronic device used for power conversion was the linear voltage regulator. In general, these devices act like a variable resistor in a voltage divider circuit. The linear regulator drops the source voltage ($V_s$) to the desired output voltage ($V_o$) by dissipating power through the variable resistor. The voltage regulator continuously adjusts the voltage divider to maintain a constant output voltage. The main problem with this method of voltage regulation is poor efficiency. The power losses in the linear regulator obey Ohm's law.

$$P_{loss} = V_{drop} I_o = (V_s - V_o) I_o \tag{2.9}$$

Switching regulators use improved power transistors (such as MOSFETs) to regulate output voltage or current. Unlike the linear regulator which uses transistor switches in a voltage divider circuit, switched-mode converters alternate between two states (either ON or OFF) through the high frequency switching of a semi-conductor or transistor switch (generally MOSFET). By controlling the time during which the switch in closed and open, the output voltage of the converter can be controlled. The duty cycle of the switch, as shown in Eq. 2.10, is the ratio of the time the switch is closed, or ON, to the total time of the switching cycle.

The converter output is controlled by adjusting this duty cycle in the acceptable range ($0 \leq D \leq 1$).

$$D = \frac{T_{\text{ON}}}{T_{\text{ON}} + T_{\text{OFF}}} = \frac{T_{\text{ON}}}{T} \tag{2.10}$$

The advantage of this ON/OFF action of the switch is a greatly improved efficiency. Roughly speaking, when the switch is in the ON state, the voltage across the resistor is zero. When the switch is in the OFF state, there is no current flowing through the MOSFETs. No voltage drop in one state and no current flow in the other results in no power losses across the MOSFET (in ideal conditions). Therefore, the switched-mode regulator is 100 % efficient in the ideal case where: the switching of the converter is instantaneous, there is no external leakage or line resistance losses, and the converter components are ideal. In reality, the components are not ideal, yet switching regulators in production today commonly have efficiencies as high as 95% [77, 48]. Yan et al. developed a bidirectional DC/DC converter for use in an electric vehicle auxiliary energy supply unit which achieved an efficiency of $> 96\%$ [78]. The details of a simple switching regulator will be discussed in a later section.

### 2.4.2 DC/DC Converters Architectures

Although much more complicated configurations exist, the simplest single-input single-output (SISO) DC/DC converters used for voltage control are the following:

- Boost converter - Increases output voltage relative to input voltage.
- Buck converter - Decreases output voltage relative to input voltage.

All DC/DC converter architectures can be derived from combinations or variations of these two standard converter topologies. DC/DC converters can vary in complexity, have multiple inputs/outputs, and control either voltage or current. They can be configured to output a fixed or adjustable voltage and are also available in bidirectional configurations capable of transferring current in both directions. Due to the variety of architectures available, the selection of DC/DC converters is highly dependent on the application.

### 2.4.3 Step-Down (Buck) Converter

DC/DC converters that are used to step-down a source voltage to a lower fixed or adjustable output voltage are referred to as buck converters. Figure 2.11 shows the electrical diagram of a buck converter. This

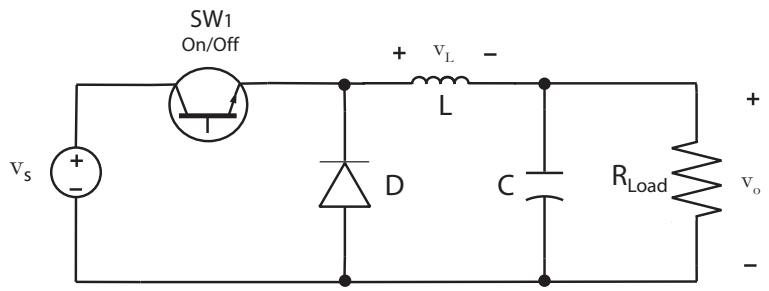


Figure 2.11: Electrical Diagram of a Buck (Step-Down) Converter.

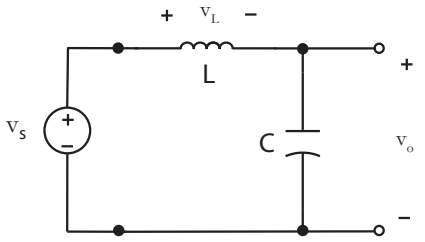


Figure 2.12: ON-State of Buck Converter.

converter accepts an unregulated DC input voltage from the source ($V_s$) and delivers a reduced, regulated, and conditioned DC output voltage ($V_o$) to the load.

When the transistor is turned ON, the converter circuit can be represented as shown in Figure 2.12. The inductor voltage is now equal to the source voltage, so the current flowing through the inductor increases and the capacitor recharges. The diode (D) is reverse biased and does not let any current flow through its terminals. The inductor current increases linearly if the voltage across it is approximately constant.

When the transistor switch is turned OFF, the converter circuit representation can be shown as in Figure 2.13. The power source is now disconnected from the circuit and the diode is forward biased and conducting current. The inductor, which resists changes in current, keeps the current flowing to deliver power to the load.

The transistor switch is rapidly turned on and off repeatedly such that the voltage and current profile across the inductor are shown by Figure 2.14. The working principle behind this device is the transfer of energy between the inductor and capacitor. With the high switching speeds delivered by the transistor switch, the inductor current remains in a linear region and changes with approximately constant slope. The LC (inductor-capacitor) circuit configuration acts like a low-pass filter, which reduces voltage ripple at fre-

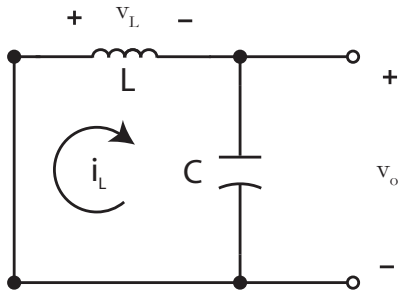


Figure 2.13: OFF-State of Buck Converter.

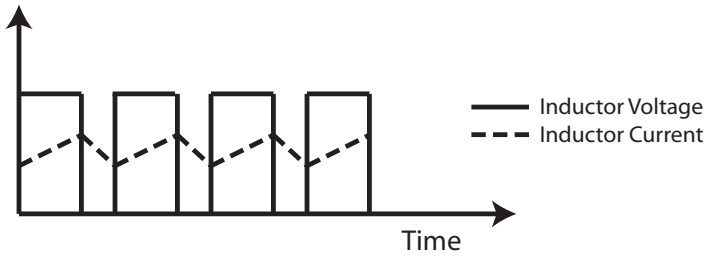


Figure 2.14: Inductor Voltage and Current.

quencies below the cutoff frequency. This filters the inductor current ripple created by the high frequency switching of the transistor and results in a constant output current to the load.

If the MOSFET switching frequency is too low, the inductor can completely discharge during the OFF cycle. This case, referred to as discontinuous conduction mode, is rare because the high frequency switching and proper sizing of the components prevent the inductor from fully discharging. In considering the operation of the DC/DC converter, only the continuous conduction mode will be considered here. Operation in this mode implies that either the diode or transistor switch is always conducting current and that the voltage across the diode is always either zero or equal to the input voltage from the source.

The simplest way to determine the input/output relationship of a DC/DC converter is to consider the inductor current over one ON/OFF cycle of the switch. Assuming that the transistor used in Fig. 2.11 is ideal and that the converter is in continuous conduction mode implies that voltage across the inductor is always the voltage difference between the source and capacitor (or load). This can be related to the inductor current as

shown in Eq. 2.11.

$$V_s - V_o = L\frac{di}{dt} \tag{2.11}$$

The total switching period ($T$) is just the sum of the time when the switch is on ($T_{\text{ON}}$) and the time when it is off ($T_{\text{OFF}}$). Assuming steady-state operation, where current is the same at the beginning of every period, Equation 2.12 can be found by breaking the integral into two parts: one when switch is ON and one when switch is OFF.

$$di = 0 = \int_0^{T_{\text{ON}}} (V_s - V_o)dt + \int_{T_{\text{ON}}}^{T} (-V_o)dt \tag{2.12}$$

By solving this integral and simplifying the results, the relationship between the switch duty cycle $D$ and the input/output voltage for the buck converter can be expressed as shown in Eq. 2.13.

$$D = \frac{T_{\text{ON}}}{T} = \frac{V_o}{V_s} \tag{2.13}$$

### 2.4.4 Step-Up (Boost) Converter

Applications where the source voltage needs to be increased requires the use of a step-up, or boost converter. Figure 2.15 shows the electrical diagram for a converter of this type. The configuration of this converter is not very different from that of a buck converter. It uses the same components, but they are arranged in a manner where the voltage output will always be higher than that of the input.

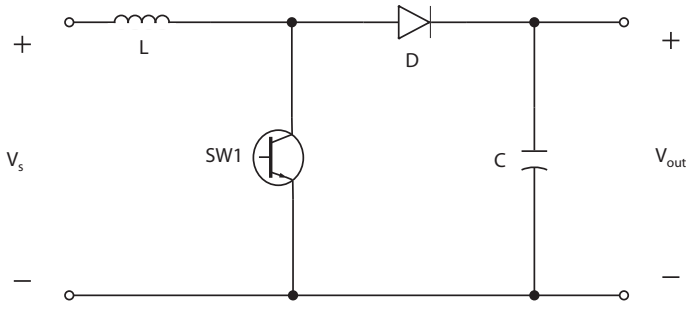


Figure 2.15: Step-Up (Boost) Converter Electrical Diagram.

When the switch is on, the diode is reverse biased and the output is isolated from the input. During

this stage, the input source is energizing the inductor, and the capacitor alone supplies current to the load. When the switch is opened, the diode becomes forward biased. The inductor supplies current to the capacitor, allowing it to charge to a higher voltage level than the input source. In this stage, the output is energized by both the inductor and the source directly. Assuming ideal components and no power losses, the relationship between the switch duty cycle and input/output voltage of the boost converter is given in Equation 2.14.

$$\frac{V_o}{V_s} = \frac{T_s}{T_{\text{OFF}}} = \frac{1}{1-D} \tag{2.14}$$

### 2.4.5 Buck-Boost Converter

The buck-boost converter topology is used in applications where the output voltage may be either increased or decreased. Figure 2.16 shows the configuration of the circuit required for this operation. The circuit is a slight variation of both the buck and boost converter circuits.

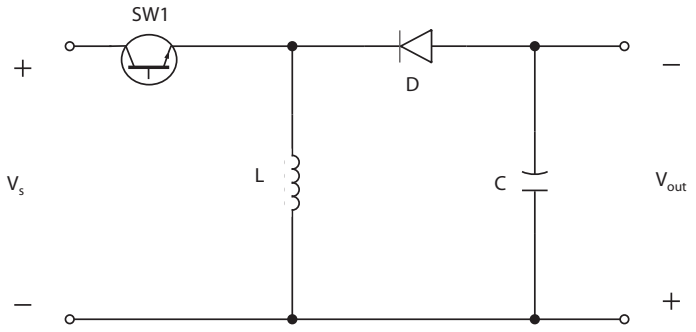


Figure 2.16: Buck-Boost Converter Electrical Diagram.

When the switch in ON, the inductor is energized by the source and an increasing current flows through it. The diode is reverse biased and the output is isolated from the input (similar to the boost converter). The load is energized only by the capacitor in this stage. When the switch is turned OFF, the diode becomes forward biased and the inductor supplies current to both the load and the capacitor. The input source is isolated from the circuit in this stage. The relationship between the duty cycle and the input/output voltage for a buck-boost converter is given by Eq. 2.15.

$$\frac{V_o}{V_s} = \frac{D}{1-D} \tag{2.15}$$

### 2.4.6 Pulse-Width Modulation

As discussed previously, the control of a DC/DC converters output voltage depends on a transistor switch which operates at a very high frequency. The most common method of controlling the switch's operation is pulse-width modulation (PWM). When using PWM for controlling the converter switch, the switching frequency is constant, and only the duration of the time the switch is ON (the pulse-width) is changed. Figure 2.17 shows a typical PWM signal which would be sent to the transistor switch.

Most DC/DC converters have integrated controllers which generate the control signal for the switch. The high-level controller supplies a reference voltage ($V_{ref}$) for the desired output voltage of the converter. The low-level controller compares the reference, or desired voltage to the actual output voltage $V_{out}$ to generate a control signal. This control signal is then sent to the transistor switch and the dynamic process continues with the control signal and output voltage continuously changing. Figure 2.17 is a general diagram showing how this control signal is generated.

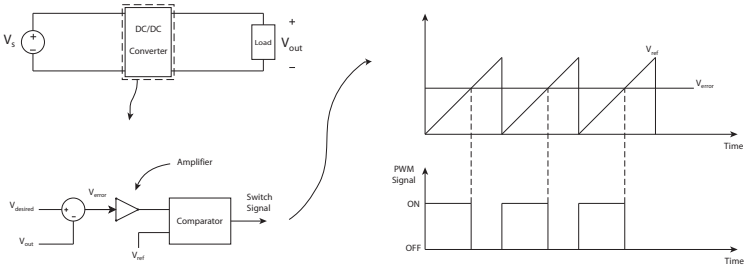


Figure 2.17: Generation of Converter PWM Control Signal.

The key to the generation of the pulse-width modulation signal is the repetitive sawtooth waveform. The frequency of this waveform becomes the frequency of the PWM signal and transistor switch. A comparator is used to compare the amplitude of the sawtooth waveform ($V_{ref}$) with the amplitude of the amplified error ($V_{error}$). If the error signal is larger than the reference waveform, the comparator returns 1, or ON. Therefore, with a larger error signal, the pulse width is increased and the voltage of the converter will approach the reference voltage. If the error signal is smaller than the reference waveform, the comparator returns a 0, or OFF. Therefore the pulse width is decreased if the error signal is small.

# Chapter 3

# Experimental Setup and Methodology

The hybrid power system considered in this paper consists of a fuel cell and ultracapacitor (UC) bank connected in parallel. An electronic load is used to draw requested amounts of power from the hybrid system. A real-time controller board is used to provide supervisory control over the system by determining the portion of the power demand met by the fuel cell (energy supply) and UC bank (energy storage). The controller implements these control actions through power electronic devices, which are used to regulate and condition the voltage and current of the fuel cell and ultracapacitor. Figure 3.1 shows a general schematic of the hybrid power system.

The fuel cell used in this setup is a Ballard® Nexa™ Fuel Cell Module. The Nexa™ fuel cell stack's 48 cells use pure gaseous hydrogen as fuel to produce unregulated DC power. The module has an on-board blower which pumps air into the stack where the oxygen is used to complete the chemical reaction. Stack temperature is maintained through the use of a cooling fan and an integrated humidifier ensures the humidity of the stack stays within a desirable operating region. This stand-alone module has a controller which implements all control actions necessary for continued operation of the stack (hydrogen valves, compressor, cooling fan, etc). The module also has emergency shut-off provisions that shuts down the stack when hazardous conditions are perceived. Some of the module output specifications are

- Peak Power: 1200 W
- Voltage at Rated Power: 26 VDC
- Current at Rated Power: 42 A

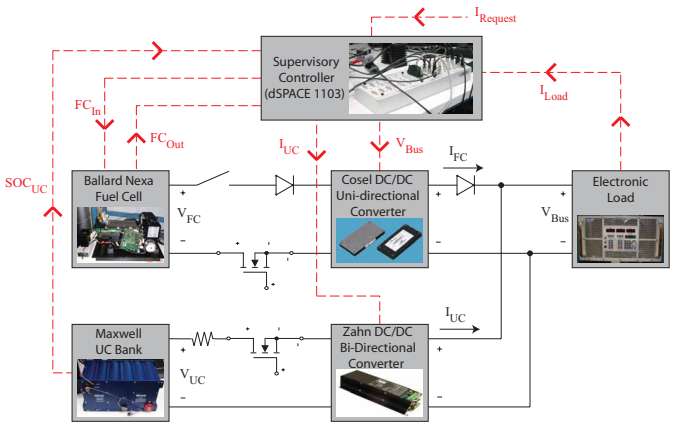


Figure 3.1: Fuel Cell/Ultracapacitor Hybrid System Schematic

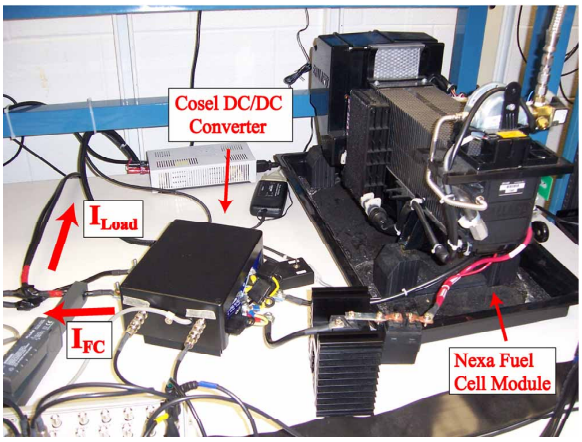


Figure 3.2: Energy Supply Side of Hybrid System

- Output Voltage Range: 22-50 VDC

The fuel cell output is unregulated, meaning the stack voltage drops as the current it provides is increased. Therefore, a power electronic device is required to maintain a steady BUS voltage. Three Cosel® *CDS*6002428 forward converters are connected in parallel in order to regulate the fuel cell output. These converters are rated for a maximum of 1800 watts and maintain a BUS voltage of 24 VDC over the entire voltage range supplied by the fuel cell module. The fuel cell and DC/DC converter combination, or the energy supply side of the hybrid system is shown in Fig. 3.2.

A single EPCOS® ultracapacitor module is connected in parallel with the fuel cell to act as a power buffer and provide energy storage. The module specifications are

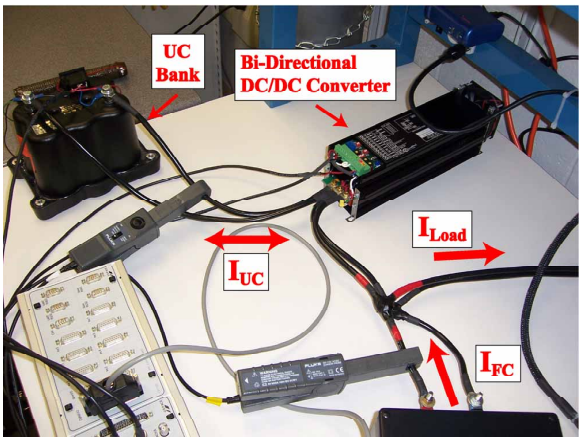


Figure 3.3: Energy Storage Side of Hybrid System

- Capacitance: 200 F
- Max Rated Voltage: 14 V
- Energy Storage: 5.44 Wh
- Peak Power Delivery: 4000 W

A Zahn® *DC*5050-*SU* DC/DC converter is used to regulate the power delivered by the UC bank to the BUS. This half-bridge converter has bi-directional current control capabilities. The acceptable input voltage range is 12-42 VDC and the maximum output power is 1200 watts. The converter can be internally powered by either the UC or the fuel cell, so that operation does not shut down as the UC voltage drops. The UC bank and DC/DC converter combination, or the energy storage side of the hybrid system are shown in Fig. 3.3.

The fuel cell and and UC bank converter work together in order to maintain a constant BUS voltage and control the current delivered by each source. The fuel cell converter operates in a voltage control mode to maintain the BUS voltage and the UC bank converter operates in a current control mode to provide supplemental current to the electronic load.

The control strategy that controls the BUS voltage and current split between the fuel cell and ultracapacitor is implemented using a dSPACE® *ds*1103 controller. The controller is first built in Simulink® , MATLAB's Real-Time Workshop® is then used to generate C-code for the the target processor. The UC voltage is sensed by voltage probes and the fuel cell and UC currents are measured using current clamps. The

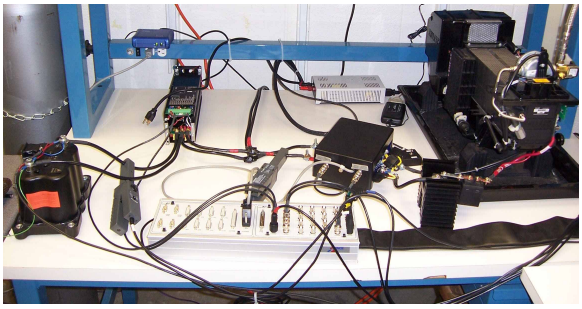

Figure 3.4: Fuel Cell/Ultracapacitor Hybrid

DC/DC converters are used as actuators to enforce the high-level control decisions. The combined system allows precise control of current delivery (at constant BUS voltage) to the load from the hybrid system. The entire hybrid power system can be seen in Fig. 3.4.

# Chapter 4

# Control Strategy Development

The control objective is to meet the power demand while minimizing fuel cell power fluctuations which helps extend fuel cell life. In order to assure that the power demand is met ($I_{BUS} \rightarrow I_D$), it is required that the sum of current supplied to the BUS by the UC and fuel cell equal the total current demand. This relationship is shown in Eq. 4.1, where positive UC current ($I_{UC}^{BUS} > 0$) represents ultracapacitor discharge.

$$I_{BUS} = I_{FC}^{BUS} + I_{UC}^{BUS} \tag{4.1}$$

Note that this relationship is only valid under the assumption of a constant BUS voltage. The fuel cell converter maintains the BUS voltage at constant $24V$, so the problem of meeting the power demand is simplified from a power split problem to a current split problem. By maintaining the BUS voltage with the fuel cell DC/DC converter, the UC DC/DC converter provides an extra degree of freedom for controlling the current split. The current demand ($I_D$) is a measured variable, so by controlling $I_{UC}^{BUS}$, the amount of current drawn from the fuel cell can be determined.

To extend the fuel cell lifetime and improve fuel economy, it is desirable to minimize the transients seen by the fuel cell. Therefore ideally we like to run the fuel cell at a constant operating point and have the UC module absorb any change in current.

Due to limitations on the size and energy storage in the UC bank, this ideal case is rarely achievable. The UC bank can exceed its maximum voltage rating at times of low demand resulting in an over-voltage condition. At times of high demand, the UC voltage may drop too low and fail to provide a cushion for future large transients in current demand. Therefore, the current the UC bank is capable of delivering depends on its

state of charge. State of charge (SOC) is simply defined as the UC voltage over its maximum rated voltage and ranges from 0 at no charge to 1 at full charge. The SOC of the UC bank becomes a key parameter when determining the current split between the two power supplies. One of the control objectives is to enforce upper and lower bounds on the UC SOC at all times.

## 4.1 Rule-Based Power Management Strategy

First a simple rule-based algorithm was devised which determines the UC current, based on the the current demand and UC's state of charge. The fuel cell supplies the difference between the current demand and the current supplied by the UC.

The difference between the current demand $I_D$ and the fuel cell desired operating current $I_{FC}^{OP}$ is passed through a first-order filter $H(s)$ to determine the desired current out of ultracapacitor, $I_{UC}^{D}$:

$$\frac{I_{UC}^{D}}{I_D - I_{FC}^{OP}} = H(s) = \frac{\tau s}{\tau s + 1} \tag{4.2}$$

where $\tau$ is the time constant of the filter. This first-order filter assures that the current delivered by the fuel cell always approaches the current demand at steady-state. This is important because the UC bank should only be considered a storage device for buffering large transients, and not as a source to provide or absorb energy for continuous periods. The speed at which the fuel cell current approaches the demand can be adjusted by the filter parameter $\tau$.

To respect the bounds on the UC's state of charge, the desired UC current is adjusted by a gain $K \in [0\ 1]$ which is a function of state of charge as shown in Fig. 4.1; that is:

$$I_{UC}^{BUS}(t) = K I_{UC}^{D}(t) \tag{4.3}$$

where $I_{UC}^{BUS}$ is the actual current that the UC should deliver to the BUS. When SOC is far from reaching a constraint, K = 1 and all the desired UC current is used, but when SOC is approaching a constraint, the gain is decreased according to the map in Fig. 4.1 until K = 0 when the SOC reaches its limits.

With only the filtering approach explained above, the ultracapacitor cannot recharge at steady-state; a recharge can only happen when the current demand goes below the fuel cell operating current. This can deplete the UC and leave it unable to absorb future transients. To avoid such a scenario, an active recharge mode is built into the rule-based controller. This mode is activated when, 1) the state of charge of the UC, and

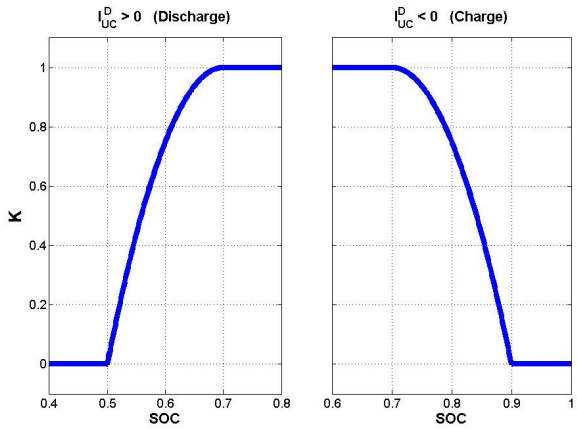


Figure 4.1: SOC Penalty Factor, K

2) the rate of change of fuel cell current are below certain thresholds. The actual values used for the active recharge are discussed next in the controller tuning section. When these conditions are met, the UC will start to draw current from the fuel cell and the current is gradually increased to a maximum charge current (adjustable).

The resulting controller provides a simple power management strategy to meet the current demanded while considering various low-level objectives and constraints, such as SOC violations. The performance of this rule-based controller was tested on the real-time platform and the results will be discussed in a later section.

### 4.1.1 Tuning of the Rule-Based Controller

The performance of the rule-based controller was largely dependent on the control parameter settings. The adjustable parameter settings include the filter time constant $\tau$ and various settings for control of the active recharge, including: the rate condition that must be satisfied before active recharge, the time delay before active charging, the duration of charge time, and the maximum charge current. Table 4.1 gives the final settings chosen for the rule-based controller that yield desired performance.

It should be noted that the rule-based controller can be adjusted to utilize the UC bank more aggressively, but this results in a quicker approach to the SOC constraints. Therefore, there is a tradeoff for how aggressively the UC bank is used and how large the effect of the SOC penalty is at constraint limits. The settings here were adjusted to perform well under relatively balanced power demand profiles.

| Parameter | Setting | Units |
|---|---|---|
| $\tau$ | 10 | Seconds |
| Max Current | 5 | Amps |
| Active Charge Duration | 20 | Seconds |
| Charge Delay | 3 | Seconds |
| $I_{FC}$ Rate Condition | 1 | Amps/second |

Table 4.1: Rule-Based Controller Settings

## 4.2 Model Predictive Power Management Strategy

The rule-based scheme works based on instantaneous current demand and state of charge of the ultracapacitor. Smoother power split decisions are expected if a predictive planning strategy is employed. In [72, 73] the merits of a model predictive control (MPC) strategy in power management of a fuel cell/ultracapacitor hybrid are demonstrated via simulation. In this thesis, the performance and the viability of implementing an MPC power management strategy are evaluated in real-time experiments.

MPC is a model-based control approach that utilizes a model of the system to project the future response as a function of control inputs and known disturbances; it then determines the optimal control inputs by minimizing a performance index over a finite prediction horizon. Pointwise-in-time constraints on the inputs, outputs, and states can be explicitly enforced in the optimization. The first control input from the calculated sequence of optimal inputs is applied to the system and the optimization process is repeated at every time step in a receding horizon fashion. When the model and constraints are linear and the performance index is a quadratic function of the states and the inputs, the MPC problem can be cast as a quadratic programming problem for which efficient solutions exist.

The predictive nature of MPC allows preemptive action to be taken if the system is approaching a constraint. This makes MPC a good candidate for the FC-UC power management problem because of the objective of reducing sharp transients in the fuel cell current while invoking the constraints on UC's state of charge. Besides, unlike the heuristic tuning in rule-based method, the MPC strategy can be tuned more systematically by adjusting the penalty weights in the performance index.

In developing a dynamic model for the MPC design, only the dynamics of ultracapacitor's state of charge are considered. Unlike in [72, 73] where explicit control of fuel cell internal states was sought, here the main criteria is controlling the current taken from the fuel cell; therefore the dynamics of the internal states of the fuel cell are not considered. The dynamics of power electronic devices are very fast and thus

neglected. In our proposed architecture, the charge and discharge of the ultracapacitor is controlled by a bi-directional dc/dc converter, conservation of energy yields:

$$\beta I_{UC} V_{UC} = V_{BUS} I_{UC}^{BUS} \tag{4.4}$$

and

$$\beta = \begin{cases} \eta_{discharge} & \text{while discharging} \\ \\ 1/\eta_{charge} & \text{while charging} \end{cases} \tag{4.5}$$

where $\eta_{charge}$ and $\eta_{discharge}$ are the charge and discharge efficiencies and assumed to be constant. The ultracapacitor effective voltage is determined by

$$V_{UC} = SOC V_{MAX} - R I_{UC} \tag{4.6}$$

where $R$ lumps the internal resistance of the UC and the resistance of the connecting cables. Assuming that the fuel cell and ultracapacitor can meet the current demand at all times, we can write:

$$I_{UC}^{BUS} = I_D - I_{FC}^{BUS} \tag{4.7}$$

where $I_{UC}^{BUS}$ is positive when the UC is being discharged and negative when being charged. Combining equations (4.4)-(4.7) we can solve for $I_{UC}$[1]:

$$I_{UC} = \frac{V_{MAX} SOC}{2R} - \sqrt{\left(\frac{V_{MAX} SOC}{2R}\right)^2 + \frac{V_{BUS}}{\beta R}(I_{FC}^{BUS} - I_D)} \tag{4.8}$$

The rate of change of state of charge is,

$$\dot{SOC} = \frac{-I_{UC}}{C V_{MAX}} \tag{4.9}$$

and therefore the state-of-charge dynamics is described by:

$$\dot{SOC} = \frac{SOC}{2RC} - \sqrt{\left(\frac{SOC}{2RC}\right)^2 + \frac{V_{BUS}}{\beta R C^2 V_{MAX}^2}(I_{FC}^{BUS} - I_D)} \tag{4.10}$$

[1]There are two possible solutions for $I_{UC}$; we retain the minimum which results in least resistive power loss.

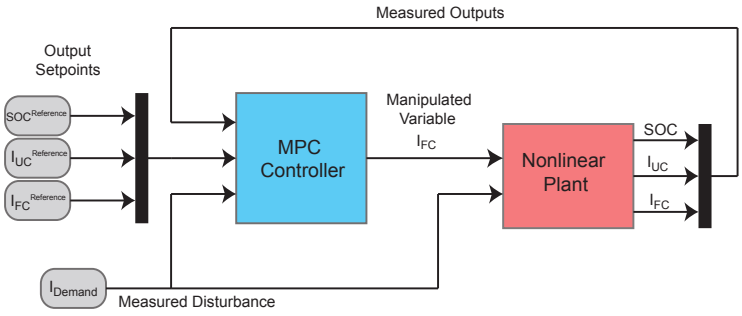


Figure 4.2: Block Diagram of MPC Controller and Linear System

For MPC design equation (4.10) is linearized around the nominal operating point where $I_{FC}^{BUS} = I_D$. The MPC objective function is chosen to be,

$$J = \sum_{j=1}^{P} (W_1 (I_{FC}^{BUS} - I_{FC}^{OP})_j^2 + W_2 (\delta SOC)_j^2 + W_3 (\Delta I_{FC})_j^2) \tag{4.11}$$

which penalizes

1. Deviations from fuel cell operating point
2. Rate of change of fuel cell current
3. Deviations in state-of-charge

with penalty weights $W_i$. To minimize the dc/dc converter losses, we enforce

$$0.5 \leq SOC \leq 0.9$$

as a hard constraint in the optimization process.

A block diagram showing the structure of the MPC optimization process through a linear model is shown in Fig. 4.2. The MPC power management scheme was developed using the MPC Toolbox in MATLAB® and implemented using a dSPACE $ds1003$ controller board in testbench experiments. More details on this process can be found in the Appendix.

### 4.2.1 Alternative MPC Controller

The MPC controller discussed previously manipulates the delivered fuel cell current as a system input. The output of this controller is the UC current. This method attempts to maintain the fuel cell current

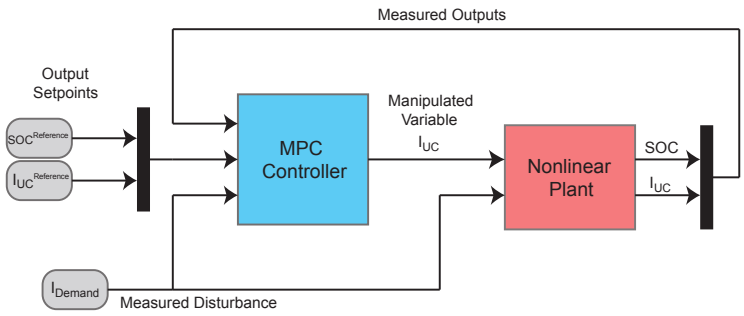


Figure 4.3: Alternative Block Diagram of MPC Controller and Linear System

near its operating point and limit fast transients seen by the fuel cell. Any difference between the current demand and fuel cell current is met by the UC bank. Considering the fact that the fuel cell model is not part of the system model used in the MPC controller development, controlling its output seems counter-intuitive.

As an alternative to the MPC controller manipulating fuel cell current, an alternative MPC controller has been developed which is based solely on the UC dynamics and manipulates the UC bank current. The controller determines the maximum amount of current that the UC can deliver within its SOC constraints. The fuel cell provides any difference between the current demand and this UC current. This method of controlling the UC current based on its own dynamics makes much more sense than controlling the fuel cell current based on the UC dynamics.

All nonlinear dynamics of the system are due to the DC/DC converters. The converter efficiencies are related to the input power in a highly nonlinear manner. Since MPC requires a linear system model, the controller developed based on the entire hybrid system had errors due to linearization of the model (nonlinearities due to power electronics). The MPC controller developed based only on the UC dynamics is linear and does not require linearization. The nonlinear system effects are imparted before the MPC controller. The maximum requested current delivered from the UC bank is first determined from the current demand, fuel cell operating point, and SOC as shown in Eq. 4.12.

$$I_{UC}^{Request} = \frac{V_{BUS}(I_D - I_{FC}^{OP})}{\beta_N V_{MAX} SOC} \tag{4.12}$$

where the $\beta_N$ is the nonlinear converter efficiency profile defined as shown in Eq. 4.13. The main advantage of this MPC configuration is that the nonlinear converter profile (determined in experimental results) can be

used for a more accurate representation of the input/output relationship through the converter.

$$\beta_N = \begin{cases} \eta_N^{discharge} & \text{while discharging} \\ \\ 1/\eta_N^{charge} & \text{while charging} \end{cases} \tag{4.13}$$

The requested current from the UC is therefore the amount of current required to supply the total BUS current demand when the fuel cell is only contributing its ideal current. Since it is desirable to maintain the SOC of the UC bank around its ideal operating point, the MPC controller determines how much of the requested current the UC can supply without violating constraints. The cost function for this MPC problem is given in Eq. 4.14. The QP problem penalizes deviations from the ideal state of charge and deviations from the requested UC bank current.

$$J = \sum_{j=1}^{P} (W_1 (SOC - SOC^{\,OP})_j^2 + W_2 (I_{UC}^{\,Request} - I_{UC})_j^2) \tag{4.14}$$

The objectives present in the cost function penalize deviations from the ideal state-of-charge ($SOC^{\,OP}$), but it is also desirable to maintain certain bounds on the $SOC$ to prevent overcharging or over-discharging. The following SOC constraint was placed on the controller to prevent these situations.

$$0.5 \leq SOC_{UC} \leq 0.9$$

The controller weights were adjusted in order to achieve performance similar to the MPC controller previously discussed. In order to achieve similar system operation, the SOC constraint had to be stiffened considerably. Comparisons on the operation of these two controllers are made in a later section.

### 4.2.2 Tuning the MPC Controllers

Tuning of the MPC strategy was more straightforward than the rule-based strategy, as the constraint on state of charge could be explicitly enforced and the power split could be adjusted through the cost function weights. No further provision was required for active recharging as opposed to the rule-based strategy. Table 4.2 lists the final penalty weights and constraints used in the MPC design based on both the hybrid system and UC dynamics. The prediction and control horizons for both controllers were set to 20 and 2, respectively.

Table 4.2: MPC Constraints and Weights.

| | Original MPC | | | Alternate MPC | | |
|---|---|---|---|---|---|---|
| Parameter | Min | Max | Weight | Min | Max | Weight |
| $SOC$ | 0.5 | 0.9 | 1000 | 0.5 | 0.9 | 550 |
| $\delta I_{FC}$ | 10 | 40 | 5 | – | – | – |
| $\Delta I_{FC}$ | $-1$ | 1 | 1 | – | – | – |
| $I_{UC}$ | – | – | – | $-\infty$ | $\infty$ | 1 |

# Chapter 5

# Experimental Results

The experimental test stand was used to test the performance of the rule-based and model predictive control strategies. Both controllers were tested in simulations and experiments. In order to test the controller's versatility under varying load profiles, several current demand scenarios were developed and are discussed next. Next, the simulation and experimental results are compared to verify the model of the closed-loop system. The closed-loop results for each controller are then presented and discussed.

## 5.1 Test Power Demand Profiles

In order to analyze the full scope of each controller's performance, operation under multiple load profiles must be considered. Initially, drive schedules published by the EPA were used along with a simple vehicle model to estimate the amount of electrical power needed for a vehicle to follow the velocity profile. The resulting power profile was scaled down by a factor of around 20 for reduced scale application on the setup in lab. Details of these drive schedules can be found in the Appendix. Although the controllers showed good performance in simulations using the drive schedules, it was found that controller performance could be more effectively measured using shorter, customized current profiles created in lab.

These profiles were implemented as current profiles drawn by the load (at constant bus voltage). Several of the profiles used for testing can be seen in Fig. 5.1. All profiles consist of a sequence of steps in the current loading which vary in frequency and amplitude. This is to test the versatility of the controllers during fast load transients.

The cycles shown in Fig. 5.1a and Fig. 5.1b are a mild and aggressive power cycles, respectively.

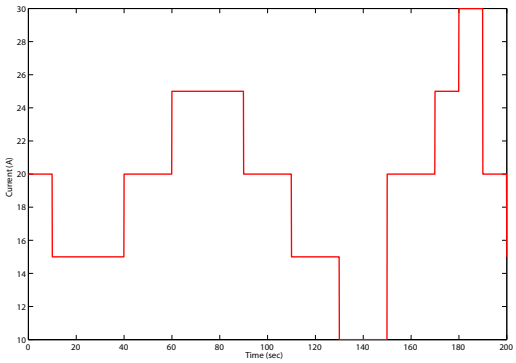


(a) Mild Cycle

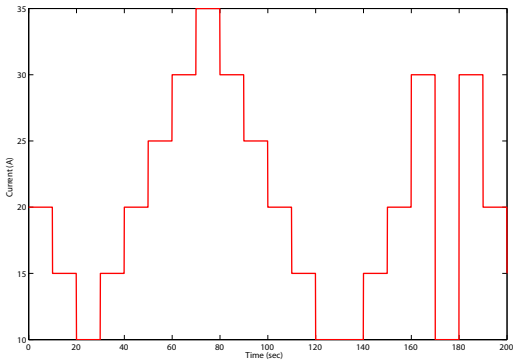


(b) Aggressive Cycle

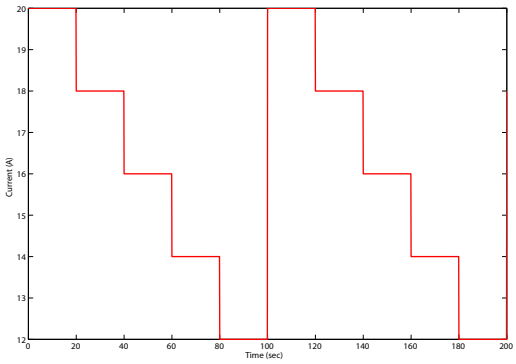


(c) Over Charge

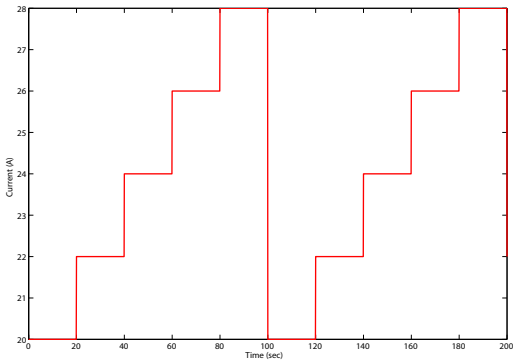


(d) Over Discharge

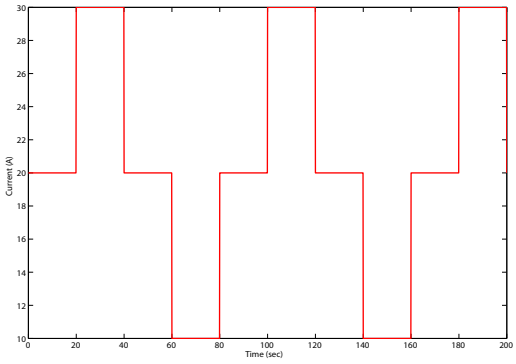


(e) Pulse (Low Frequency)

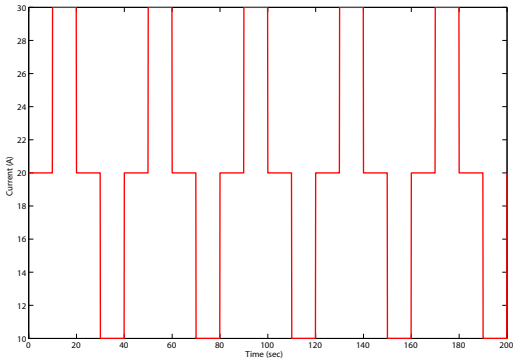


(f) Pulse (High Frequency)

Figure 5.1: Current Demand Profiles

Since the UC is utilized mostly during steps in loading, it is important to balance the number of increasing and decreasing steps in current. This is done in these two cycles, but the steps in the aggressive cycle are larger in amplitude. Figure 5.1c shows a profile which attempts to test the upper SOC constraint by overcharging the UC and the profile 5.1d tests the lower SOC constraint by over discharging. The final two, Fig. 5.1e and Fig. 5.1f, are repetitive pulses in current demand of low and high frequency, respectively.

## 5.2 Model Verification and Component Testing

Correct modeling of the individual components making up the fuel cell/ultracapacitor hybrid allows more accurate simulations and better prediction of the real-time performance under any load profile. Each component was placed under normal operation and its performance was tested. The results were used to verify the accuracy of the model for each component. The component models were then augmented into a system model for predicting the hybrid performance and tuning the controllers.

### 5.2.1 Ultracapacitor Model Verification

In order to prevent UC SOC violations, it is important to know the relationship between the UC voltage and current. The rate of change of the UC voltage can be related to the current as shown in Eq.5.1. The constant of proportionality, C, is the UC capacitance in farads.

$$I_{UC} = C\frac{dV_{UC}}{dt} \tag{5.1}$$

This expression can be easily adapted to give the SOC dynamics as shown in Eq. 5.2. Note that the negative sign is due to the chosen sign convention where a positive current represents UC discharge. The maximum rated voltage, $V_{MAX}$, is a fixed value determined by the UC manufacturer based on the breakdown voltage of the dielectric. The capacitance of the UC, which is supplied on the specification sheet, may vary over the life of the UC and must therefore be verified for accurate modeling.

$$\dot{SOC} = \frac{-I_{UC}}{CV_{MAX}} \tag{5.2}$$

A commonly used test for measuring capacitance involves charging the UC up to its rated voltage and maintaining that voltage for 30 minutes to allow the module to stabilize [49]. The UC is then discharged at a constant, low current and the time it takes for the UC voltage to drop from $0.7V_{MAX}$ to $0.3V_{MAX}$ is used to

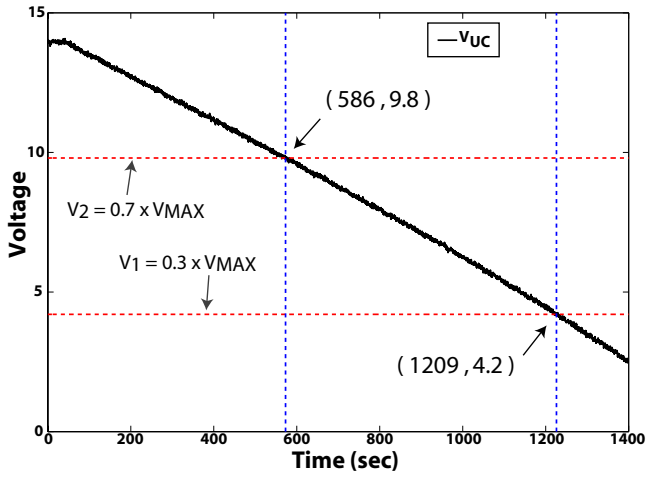


Figure 5.2: UC Capacitance Testing

give a good approximation of the UC capacitance according to Eq. 5.3. This method is based on the fact that constant current discharge of a constant capacitance UC should result in a linear voltage profile. Figure 5.2 shows the results of this method when used to test the UC used in the setup in lab. The discharge current in this case was a constant 2 amps.

$$C \approx \frac{I \cdot (T_2 - T_1)}{V_2 - V_1} \tag{5.3}$$

For the EPCOS® ultracapacitor we tested, the specification sheet states that the capacitance value is 200 farads, but the test shows that a more accurate value is 222 farads. In order to verify this result, the UC was connected directly to an electronic load and a simple step in current is administered. The current and voltage of the capacitor were measured and the results were compared with simulation results based on the UC model. The simulation was performed twice, once for each capacitance value, and the results were compared. The results, as seen in Fig. 5.3 show that a capacitance of 222 farads results in more accurate prediction of the UC voltage under constant current discharge and is therefore the capacitance value used in modeling the UC.

### 5.2.2 Bidirectional Converter Efficiency

The model of the bidirectional DC/DC converter which is used to connect the UC bank to the BUS was verified next. Since the converter just serves as an energy conversion device, the model involves de-

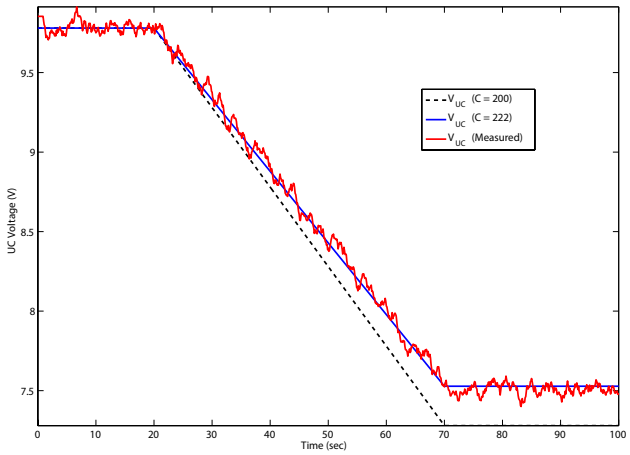


Figure 5.3: UC Capacitance Value Verification

termining an efficiency map. The converters bidirectional current control function complicates creation of a simple efficiency map. Efficiency is the ratio of power going into the converter to the power coming out of the converter, but in a bidirectional converter, the input and output source may change, receiving input power from the fuel cell when charging and from the UC when discharging the UC bank. This unique operation results in a switching nonlinearity in the efficiency calculations. In order to model this switching nonlinearity, the efficiency of the bidirectional converter is represented as shown in Eq. 5.4.

$$\eta^{sgn(I_{UC})} I_{UC} V_{UC} = I_{BUS} V_{BUS} \tag{5.4}$$

The efficiency map, relating input power to efficiency, was found empirically through testing of the converter. This testing showed that the efficiency was dependent on input power and the efficiency map was the same both when the UC bank was the input source (discharging) and when the fuel cell was the input source (charging). This map was generated considering only input power levels and did not consider all possible voltage/current combinations. The relationship between converter efficiency and input power is shown in Fig. 5.4.

### 5.2.3 Fuel Cell Efficiency

In order to complete the model verification, the efficiency of the fuel cell side must now be determined. Testing performed on the setup in lab (see Section 2.1.4) has shown that the Nexa$^{TM}$ fuel cell module

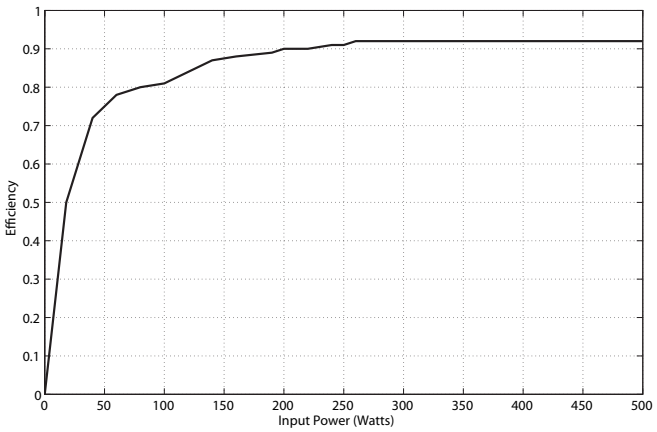


Figure 5.4: Bidirectional DC/DC Converter Efficiency Map

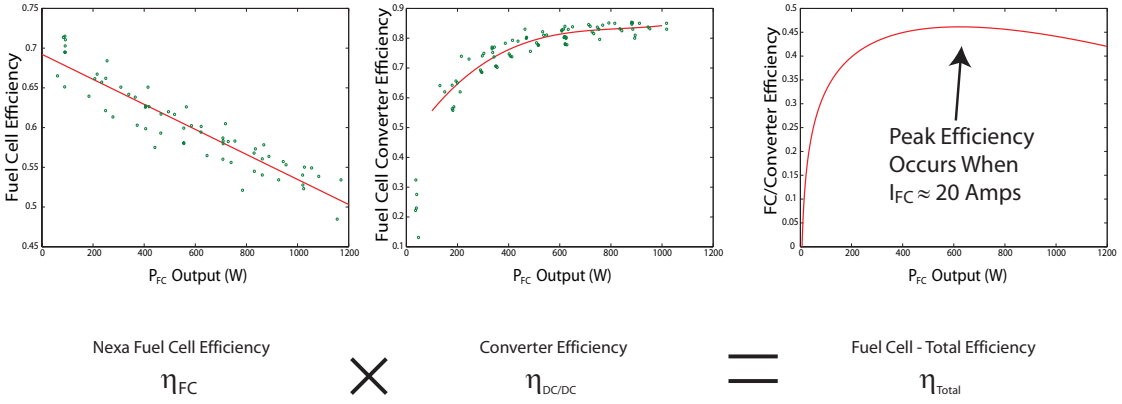


Figure 5.5: Fuel Cell/Converter Combined Efficiency

efficiency is inversely proportional to the amount of power drawn from the stack. The results of this testing can be seen in the first plot of Fig. 5.5, where increasing the fuel cell output power results in decreased efficiency. Since the fuel cell output voltage drops as current increases, a DC/DC converter is needed to regulate the output to a constant voltage BUS. Since the efficiency of the DC/DC converter has increased efficiencies at higher power levels (as shown in the second plot in Fig. 5.5), the combination of these two devices results in a fuel cell side efficiency curve with a maximum efficiency point. Figure 5.5 shows the efficiency plot of the fuel cell side of the hybrid.

This maximum efficiency occurs when the fuel cell is delivering approximately 20 Amps to the 24 volt BUS. Therefore, fuel consumption can be minimized by attempting to maintain the fuel cell around this

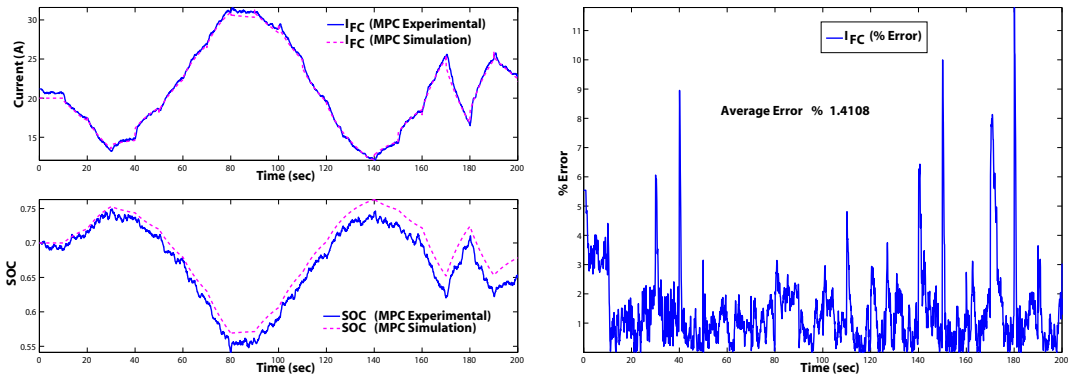


(a) Comparison

(b) Error Analysis

Figure 5.6: Simulation vs. Experimental Results: MPC

operating point. This is achieved by penalizing the deviation of $I_{FC}$ from $I_{FC}^{OP}$ in the MPC cost function and not directly enforced in the rule-based controller. Although the fuel cell side model is not used in making control decisions, modeling it helped in the determination of the most efficient operating point.

### 5.2.4 Closed-Loop System Model Verification

The component models discussed in the previous sections were combined to create a complete simulation model used to predict the response of the actual system under various current demand profiles. The aggressive current demand profile from Fig. 5.1b which includes large transients and extended high and low power segments was used to verify the model used for simulation. The accuracy of the closed-loop simulation model was verified by also running the controller on the experimental system and comparing the results to those of simulation. Figures 5.6 and 5.7 show a comparison of the simulation and experimental results for the two control methods used; a rule-based and a model predictive power management strategy.

Figure 5.6a shows the simulated and experimental results for the fuel cell current (top) and UC SOC (bottom) when the MPC strategy was used. The deviations between the simulation results (purple dotted line) and the measured experimental results (solid blue line) are relatively small. An error analysis of the fuel cell current (shown in Fig. 5.6b) shows the absolute percent error between the experimental and simulation results. The average error over the entire cycle was only 1.41% with the maximum error reaching 12%.

Figure 5.7a shows the simulated and experimental results for the fuel cell current (top) and UC SOC (bottom) when the rule-based strategy was used. The deviations between the simulation results (orange dotted

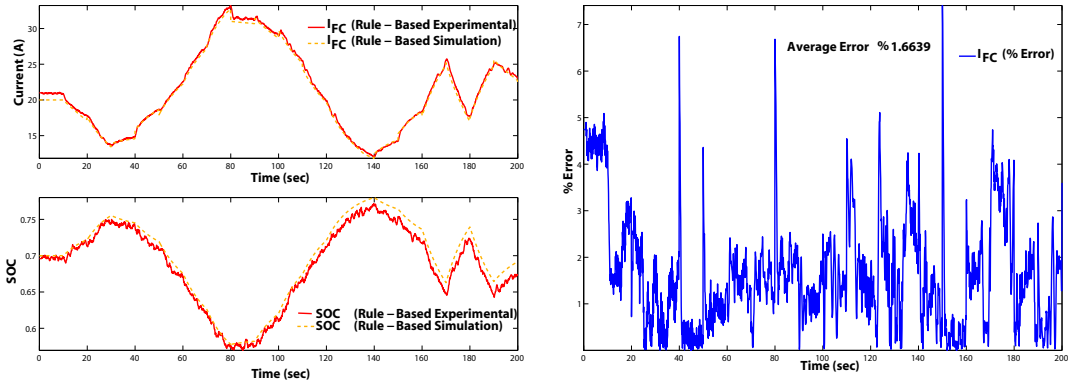


(a) Comparison

(b) Error Analysis

Figure 5.7: Simulation vs. Experimental Results: Rule-Based Control

line) and the measured experimental results (solid red line) remain small. An error analysis of the fuel cell current (shown in Fig. 5.7b shows the absolute percent error between the experimental and simulation results. The average error over the entire cycle was only 1.66% with the maximum error reaching 8%.

Any of the small differences between the experiment and simulation results are most likely due to unmodeled losses in the system. The line resistance losses are relatively small, but could have an influence on the experimental output. The bidirectional converter's nonlinear efficiency map could also be a source of error as it was difficult to model accurately.

## 5.3 Closed-Loop Results: Rule-Based Controller

The closed-loop system performance under rule-based control was tested by running the system through various load profiles. Although performance under various profiles was tested, all examples shown in the figures here are based on the aggressive drive cycle (Fig. 5.1b). This cycle was chosen because it pushes the system to meet both high and low current levels and fast transients in current. The current split enforced under the aggressive drive cycle is shown in Fig. 5.8. The solid black profile represents the BUS current, $I_{BUS}$, which was drawn from the hybrid system from the electronic load. Based on the current demand and SOC of the UC, the controller actuates the bidirectional converter to control the amount of current supplied by the UC bank. The dotted red line is the UC current as measured from the BUS, $I_{UC}^{BUS}$. The difference between the current demand and UC BUS current must be provided by the fuel cell and is shown in the figure as the solid blue line.

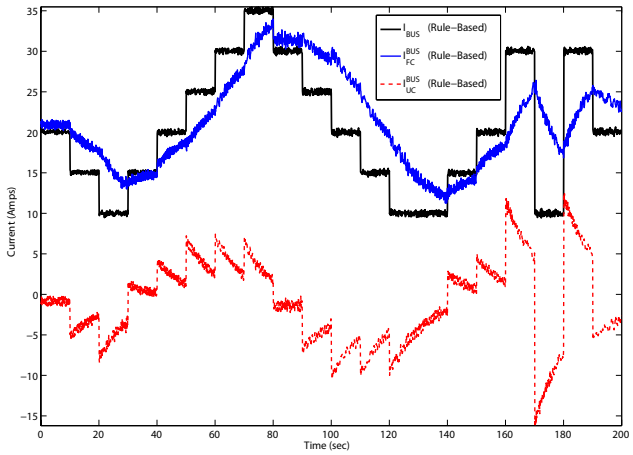


Figure 5.8: Closed-Loop Current Split: Rule-Based Control

The UCs ability to provide sharp transients in current is evident from Fig. 5.8. When there is a step down in the BUS current, the UC quickly absorbs the change in current, allowing the fuel cell to slowly transition towards the new current demand. When there is a step up in BUS current, the UC quickly delivers current and slowly decreases its contribution as the fuel cell slowly increases its output to meet the demand. If the BUS current is held constant long enough, the fuel cell approaches this current level as the UC current drops to zero.

Figure 5.9 gives another representation of this process where the UC bank absorbs the large transient currents. The top plot in the figure shows the same current demand and fuel cell current shown previously, while the bottom plot shows the SOC of the UC over the same load profile. It is interesting to note that the SOC looks like a scaled mirror image of the fuel cell current. When the fuel cell current is decreasing, the BUS current is lower than the fuel cell current. This difference results in charge current going to the capacitor and therefore the increase in SOC. It is in this manner that the SOC always counter-balances the fuel cell current, allowing smoother fuel cell operation. This current buffering action will occur until a constraint violation on the SOC of the UC is approached, meaning the UC cannot absorb or deliver any more current. When this happens, the fuel cell must provide the current that the UC can not provide.

The effect of approaching an SOC violation can result in large current spikes in the rule-based strategy. Figure 5.10 shows simulation results of the fuel cell current, $I_{FC}$, over the same current demand profile for two cases; one when rule-based strategy assumes no limits on the ultracapacitor state-of-charge (uses $K = 1$) and the other when K is determined using the map Fig. 4.1. In reality, the UC voltage has

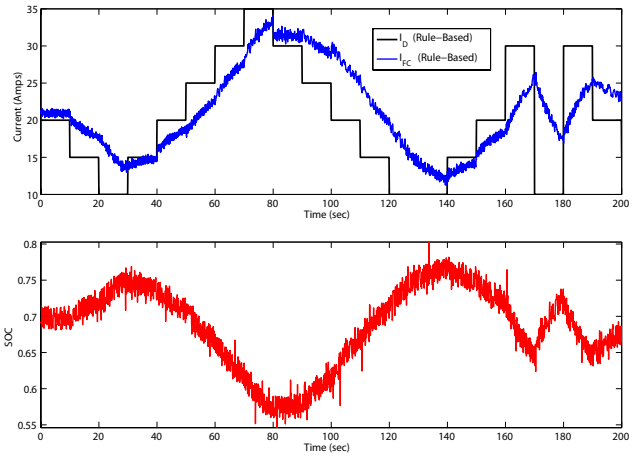


Figure 5.9: Experimental Results: Rule-Based Control

limitations that must be enforced, so K will sometimes be less than 1. It is in these cases, where the SOC is approaching a constraint that the UC must limit its contribution and the fuel cell current sees sharp transients as a result. In Fig. 5.10, the most noticeable example of this occurs around 80 seconds, when the fuel cell must absorb a large portion of the current change as the BUS demand is stepped down from 35 to 30 amps. This kind of transients is not desirable and if happens frequently may be even detrimental to fuel cell life. Also authors of [73] show that such transients may cause air compressor surge instability when a high-pressure PEM fuel cell is used.

## 5.4 Closed-Loop Results: Model Predictive Controller

The closed-loop system performance with model predictive control was tested in the same manner as the rule-based controller. The aggressive drive cycle (Fig. 5.1b) is used here to show the controller performance, and the current split under this cycle is shown in Fig. 5.11. The solid black profile represents the BUS current, $I_{BUS}$, which was drawn from the hybrid system from the electronic load. The model predictive controller used the linear system model to predict future system responses and optimizes a cost function to determine the proportion of current that should be delivered by the UC bank. The dotted red line is the UC current as measured from the BUS, $I_{UC}^{BUS}$. The difference between the current demand and UC BUS current must be provided by the fuel cell and is shown in the figure as the solid blue line.

As shown in Fig. 5.11, the UC bank quickly charges or discharges current when the current de-

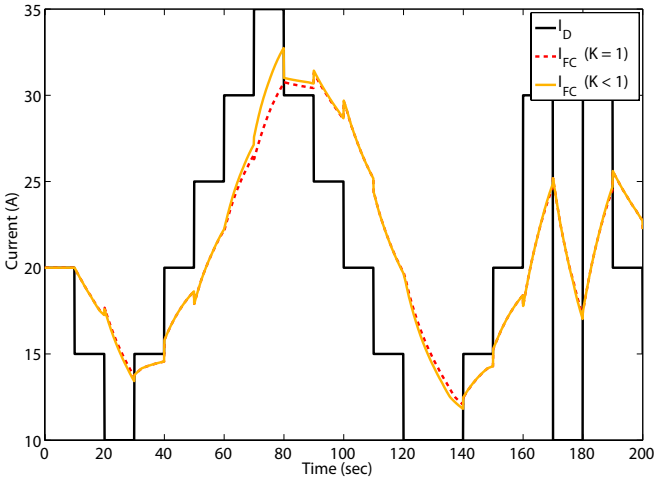


Figure 5.10: SOC Penalty Effect

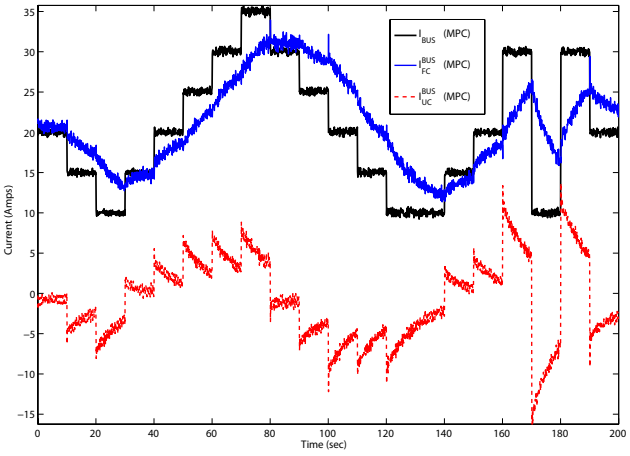


Figure 5.11: Closed-Loop Current Split: MPC

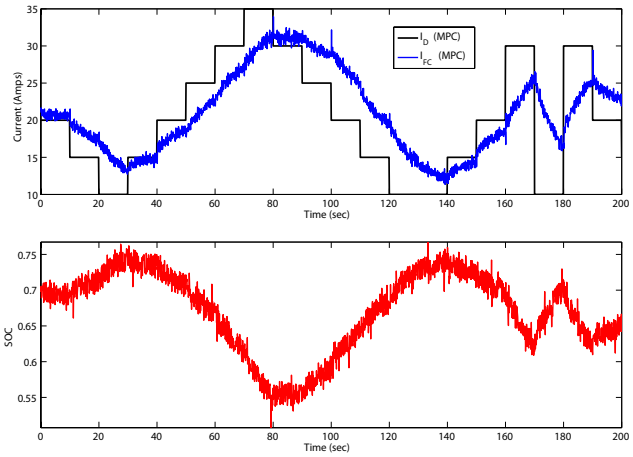


Figure 5.12: Experimental Results: MPC

mand is stepped down or up, respectively. This buffering action allows the fuel cell to slowly approach the demanded current level and reduces sharp changes in current the fuel cell must provide.

Figure 5.12 gives another representation of this process where the UC bank absorbs the large transient currents. The top plot in the figure shows the same current demand and fuel cell current shown previously, while the bottom plot shows the SOC of the UC over this profile. The SOC profile once again looks like a mirror image of the fuel cell current.

## 5.5 Rule-Based and MPC Closed-Loop Results

In order to gain insight into pros and cons of MPC strategy versus rule-based the results are more closely compared. The current demand profile chosen for this study is the aggressive cycle profile (Fig. 5.1b). The UC bank was given an initial charge and the current profile was applied for the hybrid system under each of the two controllers. Figure 5.13 shows the fuel cell current with each controller. The solid black line is the current demand, the solid red line is the measured fuel cell BUS current using the rule-based controller, and the blue dotted line is the measured fuel cell BUS current under the MPC controller. This plot shows a close resemblance between the performance of the two controllers. There is an offset in the fuel cell current during the first 20 seconds. The nominal fuel cell current, $I_{FC}^{OP}$, is 20 amps and the fuel cell current (for both controllers) begins at around 21 amps. This 1 amp difference is most likely due to the fact that the fuel cell is providing not only the BUS current, but it is also powering the UC side converter during this time. The

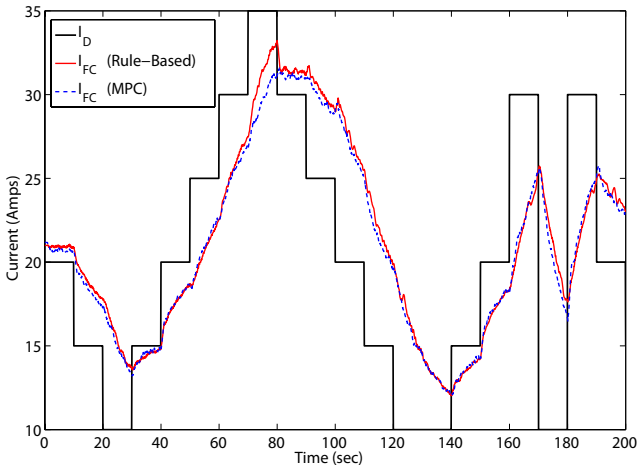


Figure 5.13: MPC vs. Rule-Based Control: Fuel Cell Current Comparison

largest deviation between the two fuel cell currents occurs between 70 and 80 seconds. This deviation is due to the fact that a SOC constraint is being approached and the rule-based controller reduces the amount of UC bank current supplied.

Figure 5.14 shows a comparison of how the UC bank was utilized by each controller under the aggressive current demand profile. Once again, it is noticeable that the controllers have very similar performance. The main deviation occurs between 70 and 80 seconds, when the UC SOC is approaching a constraint and the rule-based controller reduces the current it can supply. Both controllers absorbed the transients equally well until the SOC penalty effect limited the rule-based supply current.

The rule-based controller was more conservative in using the UC bank to supply current while the MPC controller was more aggressive. This can be easily seen in Fig. 5.15 where the MPC controller quickly approaches constraints without violating them. The rule-based controller could be tuned to act in a more aggressive manner, but this results in an abrupt decrease in the magnitude of UC current when a constraint is reached, leaving any other changes in loading to be absorbed by the fuel cell.

Overall, the MPC controller's predictive nature results in smoother transitions in current delivered by the fuel cell and smaller deviations from nominal fuel cell current. The simplicity and ease of implementation of the rule-based controller may make it also a viable candidate for applications which have less stringent performance constraints.

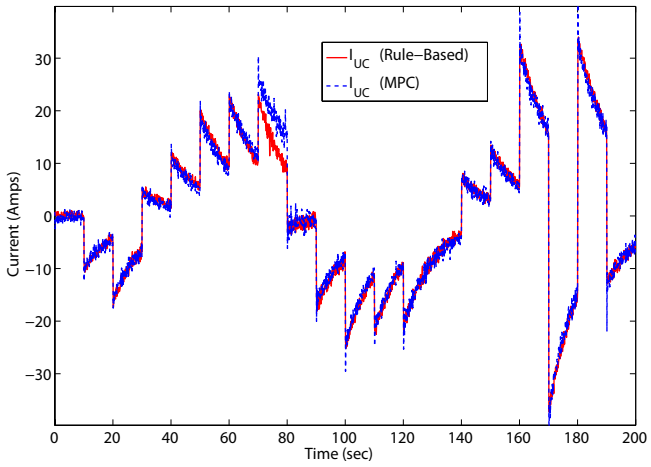


Figure 5.14: MPC vs. Rule-Based Control: UC Current Comparison

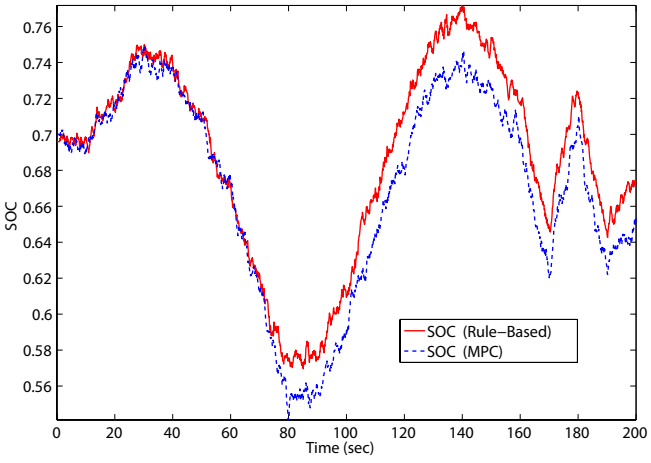


Figure 5.15: MPC vs. Rule-Based Control: UC SOC Comparison

| Case | $\delta I_{UC}^{Request}$ Weight | *SOC* Weight |
|---|---|---|
| High SOC Penalty | 1 | 1500 |
| Low SOC Penalty | 1 | 400 |

Table 5.1: MPC Weighting: High and Low SOC Penalty

## 5.6 Influence of MPC Design Parameters on Performance

The cost function which is used to find the optimal control actions in model predictive control can be adjusted to change the controller performance. One method of tuning the performance of these controllers is changing the penalty weighting and another is through adjustment of the prediction and control horizons. The effects of each of these changes are shown in the next two sections.

### 5.6.1 Penalty Weighting

The effect of changing the weights of the MPC controller is shown here through real-time results from the MPC controller. The two weights in the cost function are on the deviation from the requested UC current ($\delta I_{UC}^{Request}$) and the deviation from the ideal SOC. The weight on $\delta I_{UC}^{Request}$ was held constant and the weight on SOC was varied to show the effects of different weighting. The relative weighting, not absolute weighting, is important in the MPC problem. Table 5.1 shows the two different weighting cases.

The effects of the large SOC penalty can be seen in Fig. 5.16. Such a large penalty on the SOC deviation results in very little use of the UC. The relative weighting can be adjusted for more aggressive or conservative performance depending on the application.

Figure 5.17 also shows the effect a large SOC penalty has on the current split in the system. In the case of the large penalty, the UC bank is hardly used as a buffer, forcing the system to rely mainly on the fuel cell to provide the demanded power.

### 5.6.2 Prediction and Control Horizons

Adjusting the prediction and control horizons is another method by which the performance of MPC controller can be tuned. Simulations were used to examine the effects of changes in these horizons. The MPC controller discussed previously was used for power management under a simple pulse current demand profile. The control horizon was maintained at a constant value of 2 and weights were held constant. The prediction horizon was adjusted from short to long and the simulation results were recorded.

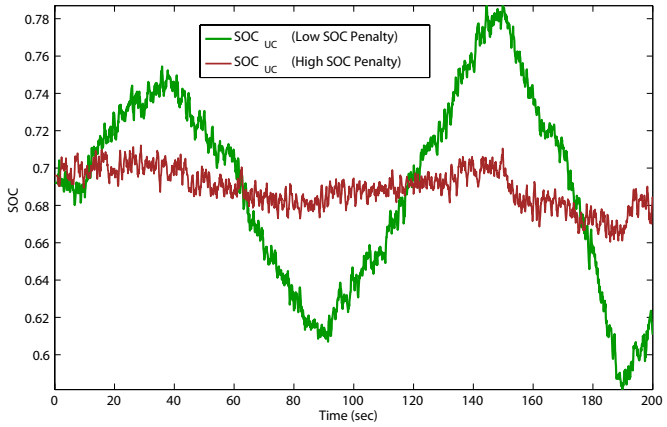


Figure 5.16: SOC Weighting Effect

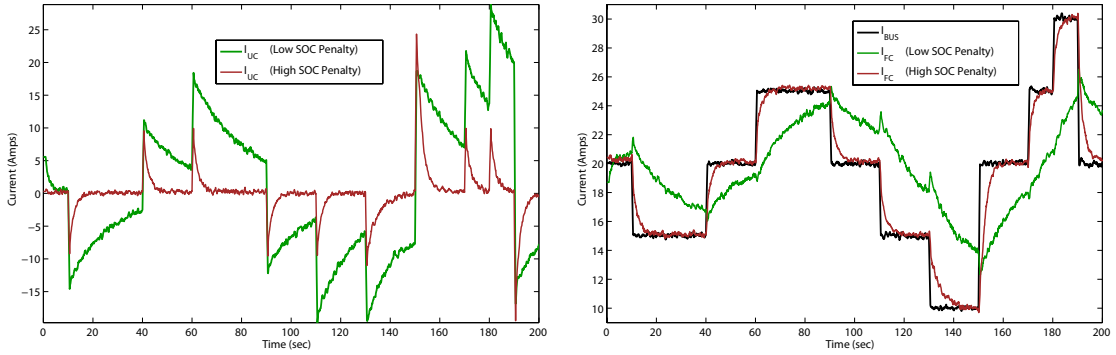


Figure 5.17: SOC Weighting Effect: $I_{UC}$ & $I_{FC}$

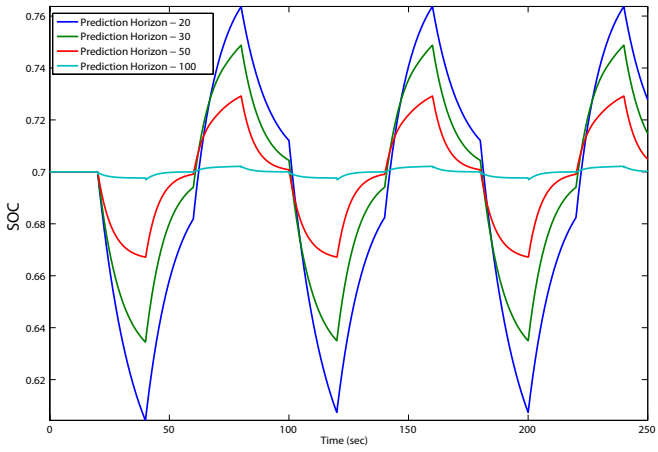


Figure 5.18: SOC Under Varying Prediction Horizon

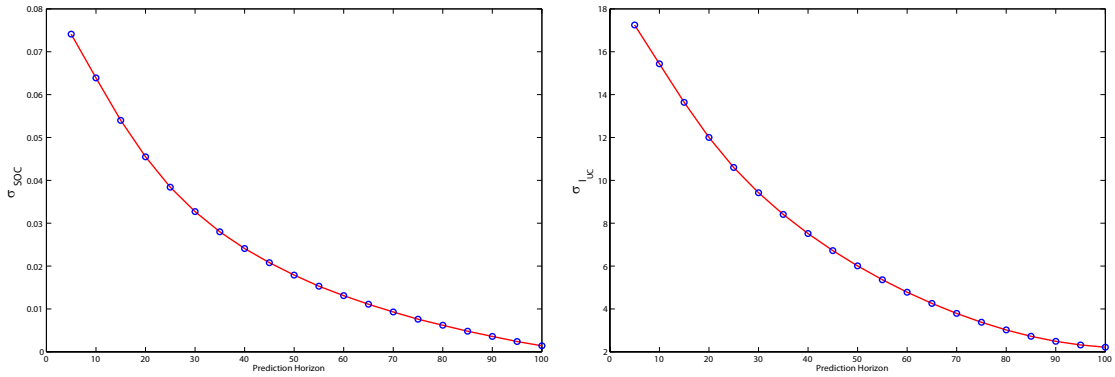


Figure 5.19: UC Bank Usage Under Constant Control Horizon and Varying Prediction Horizon

Figure 5.18 shows the state of charge of the UC under the various prediction horizons. From this plot, it can be seen that the UC bank is used in a more aggressive manner with a shorter prediction horizon. The reason for this may be that with a longer prediction horizon, the anticipation of a SOC constraint violation results in more conservative use of the UC bank and smaller deviations in SOC.

Figure 5.19 shows the standard deviation of the state of charge and current of the UC bank. It can once again be seen that a longer prediction horizon leads to decreased usage of the UC bank. Because of the wide variations in SOC under a small prediction horizon, the controller tends to perform poorly when reaching a constraint, but a long prediction horizon does not utilize the UC bank to its full advantage. Through trial and error for this particular application, a prediction horizon of 20 and control horizon of 2 produced the best results (based on sampling time of 0.1 seconds).

# Chapter 6

# Conclusions and Future Work

It has been demonstrated that model predictive power management of a fuel cell/ultracapacitor hybrid results in improved system performance as compared to a rule-based strategy. The fuel cell current changes more smoothly with fewer sharp transients in loading which is expected to help the fuel cell durability and improve fuel economy. Due to explicit handling of the state-of-charge (SOC) constraint in model predictive control (MPC), the UC bank is used more aggressively to buffer sharp transients and supply power in times of high demand. The rule-based controller does not always fully utilize the power available from the UC bank. Furthermore the MPC is shown to be real-time implementable for this type of application which requires a relatively fast sample time of 0.1 seconds.

The biggest advantage of the model predictive control strategy may lie in its versatility and ease of tuning. The rule-based controller needs retuning if a different type of demand profile is expected while the optimization-based and predictive nature of MPC makes it applicable across a wide range of demand profiles. The choice of a prediction horizon for the MPC controller showed great influence on the system performance, where a larger horizon resulted in better anticipation of constraints and more conservative use of the UC bank. No correlation between the control horizon and system performance was observed in simulations, stimulating the need for further investigation into its effects. Overall, the MPC scheme enables more systematic control of the hybrid system, and ensures better load-following and possibly longer fuel cell stack lifetime.

One possible extension of this work currently being considered is the utilization of a rule-based strategy at a supervisory level for coordination and MPC at low-level for constraint enforcement. This decentralized architecture could allow for modular controller implementation, splitting the high-level and low-level control decisions into two separate, but communicating controllers.

The hybrid system architecture is also an area where research could lead to configurations offering better performance and fuel economy. The inclusion of a battery pack in coordination with the UC may serve as a better energy storage device for fuel cell hybridization. The use of two DC/DC converters was chosen because it provides active current and voltage control. It is possible that through correct component sizing, the system could be operated with only one converter, reducing the cost and losses of an additional converter.

# Appendices

# Appendix A MATLAB® MPC Controller Files

## A.1 MPC Control: Simulink Model

Figure 1 shows the Simulink® model used for the real-time implementation of the model predictive controller. The controller was developed using the mpctool available through MPC Toolbox™ . An MPC object was created which operates through an s-function. The model was compiled using Real-Time Workshop® to the dSPACE® ds1103 controller board.

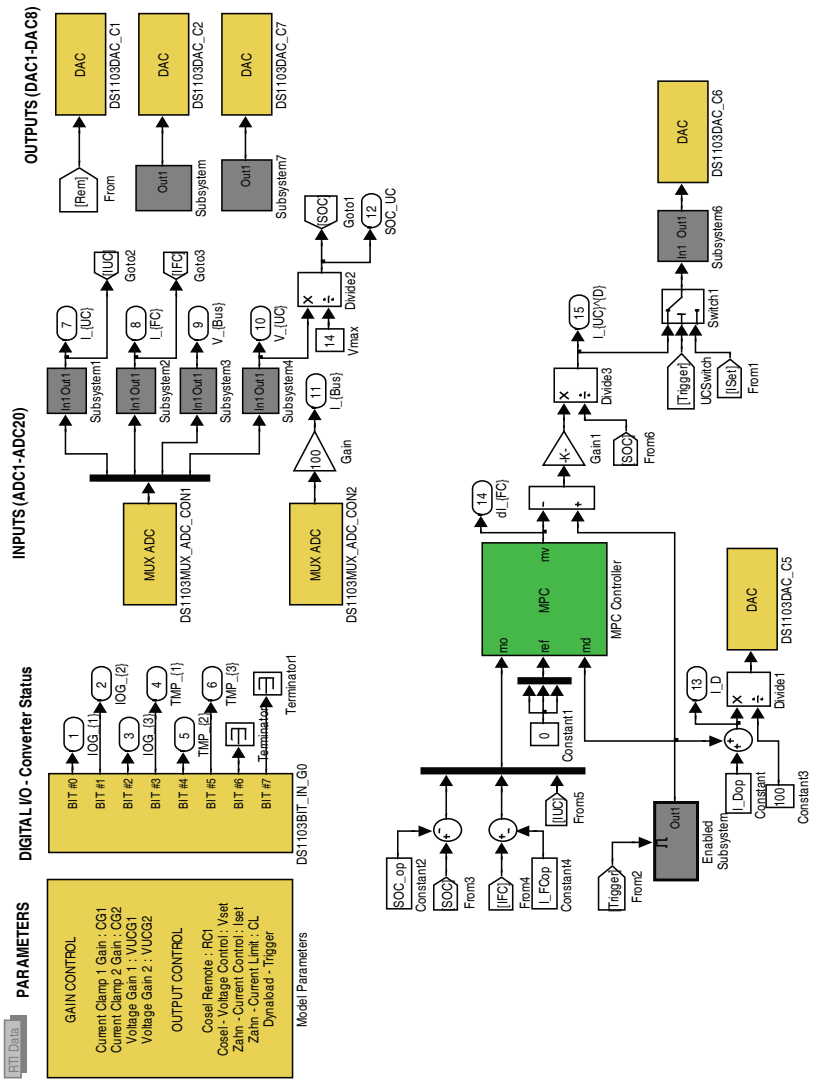


Figure 1: MPC Controller - Simulink® Model.

## A.2 Controller Interface: mpctool

The mpctool provides a graphical user interface where an MPC controller can be created and altered. Using the tool, the linear system model can be imported from the workspace and the various inputs and outputs can be classified in one of the following categories: measured or unmeasured outputs, measured or unmeasured disturbances, and manipulated variables (control inputs). The user can then develop a controller and adjust many parameters including the following: prediction horizon, control horizon, sampling time, constraints, and weighting. When finished, the tool compiles all controller and model information in an object to be used by the s-function. Some of the data contained in the MPC object is shown in Fig. 2.

```
>> load MPC1
>> MPC1

MPC object (created on 06-Mar-2008 10:07:29):
-------------------------------------------------
Sampling time:      0.1
Prediction Horizon: 20
Control Horizon:    2

Model:
         Plant: [3x2 ss]
       Nominal: [1x1 struct]
   Disturbance: []
         Noise: []

      Output disturbance model: default method (type "getoutdist(MPC1)" for
details)

Details on Plant model:
                              --------------
     1  manipulated variables   -->|  3 states  |
                                |           |--->  3 measured outputs
     1  measured disturbances   -->|  2 inputs  |
                                |           |--->  0 unmeasured outputs
     0  unmeasured disturbances -->|  3 outputs |
                              --------------

Indices:
  (input vector)    Manipulated variables: [1 ]
                 Measured disturbances: [2 ]
  (output vector)       Measured outputs: [1 2 3 ]

Weights:
       ManipulatedVariables: 7
    ManipulatedVariablesRate: 3
          OutputVariables: [900 0.1000 0.1000]
                  ECR: 1.0000e+005

Constraints:
 -10 <= dI_FC <= 20, -0.1 <= dI_FC/rate <= 0.1,     -0.2 <= dSOCo <= 0.2
                                    dI_FCfo is unconstrained
                                    dI_UCfo is unconstrained
>>
```

Figure 2: MPC Object Generated by MPC Toolbox$^{TM}$ .

## A.3 MATLAB® m-file for Loading Controller

An m-file was used to prepare MATLAB® workspace for running the toolbox. The m-file loads all pertinent variables, models, and load profiles. The model is then compiled using Real-Time Workshop from the model. Page 1 of the m-file used to set up the MPC controller Simulink™ model is Fig. 3.

```
3/25/08 8:30 AM  C:\dSPACE-Experiments\Hybrid_Control\MPC\run_mpc_hybrid.m          1 of 2

%% Run mpc_hybrid
clear all; close all; clc;
%% System Parameters and Simulation Times
tf=200;
dt=0.1;
tvec=[0:dt:tf]; tau=2*dt;
Cf=200; Vmax=14; Vbus=24; R=.1; eta=.85;
%% Operating Point Linearization Coefficients
SOC_op=0.7; I_Dop=20; I_FCop=20;

alpha1=-1/(2*R*Cf)+SOC_op/sqrt((2*R*Cf*SOC_op)^2+...
    ((16*R^3*Cf^2*Vbus)/(eta*Vmax^2))*(I_FCop-I_Dop));
beta1=Vbus/sqrt((eta*Cf*Vmax^2*SOC_op)^2+...
    4*eta*R*Cf^2*Vmax^2*Vbus*(I_FCop-I_Dop));
gamma1=-beta1;
%% State Space Model (Hybrid)
A1=[alpha1 0 0;0 -1/tau 0;alpha2 0 -1/tau];
B1=[beta1 gamma1;1/tau 0;beta2 gamma2];
C1=[1 0 0;0 1 0;0 0 1];
D1=0;
mysys=ss(A1,B1,C1,D1,'statename',{'dSOC','dI_FCf','dI_UCf'},...
                         'inputname',{'dI_FC','dI_D'},...
                         'outputname',{'dSOCo','dI_FCfo','dI_UCfo'});
%% Load and Alter MPC Object
load MPC1
w.ifc = 7;
w.ifc_rate = 3;
w.dsoc = 1500;
w.ifcf = .1;
w.iucf = .1;
MPC1.PredictionHorizon=20;
MPC1.ControlHorizon=2;
MPC1.Weights.ManipulatedVariables=[w.ifc];
MPC1.Weights.ManipulatedVariablesRate=[w.ifc_rate];
MPC1.Weights.OutputVariables=[w.dsoc,w.ifcf,w.iucf];
%% Current Demand (Steps)
over_charge=[15 10 15 20 25 30 35 30 25 20 15 10 15 20 15 10 10 10 10];
over_discharge=[15 10 15 20 25 30 35 30 25 20 15 10 15 20 30 30 30 30 30];
mix_cycle=[15 10 15 20 25 30 35 30 25 20 15 10 10 15 20 30 10 30 20];
pulse_cycle=[20 15 25 15 25 15 20 30 10 30 10 30 10 30 25 20 15 20 20];
mild_cycle=[15 15 15 20 20 25 25 25 20 20 15 15 10 10 20 20 25 30 20];
idemvec=mix_cycle-I_Dop;
steptime=10;
inputdelay=0;
%% Load Drive Cycle Data
% steptime=1;
% vbusdes=400;
% % filename = 'IM240';     % Inspection and Maintenance Drive Schedule
% % filename = 'HWFET';     % Highway Fuel Economy Drive Schedule
% % filename = 'UDDS';      % Urban Dynamometer Drive Cycle
% % filename = 'NYCC';      % New York City Cycle
% % filename = 'EPA75';     % EPA Federal Test Procedure
```

Figure 3: M-File for Running MPC Controller.

Page 2 of the m-file used to set up the MPC controller Simulink$^{TM}$ model is Fig. 4.

```
3/25/08 8:30 AM  C:\dSPACE-Experiments\Hybrid_Control\MPC\run_mpc_hybrid.m          2 of 2

% filename = 'US06';      % High Acceleration Aggressive Drive Cycle
% file=char(strcat('C:\dSPACE-Experiments\Hybrid_Control\Drive_Schedule_Current\',↙
filename));
% load(file);
% demand(:,2)=demand(:,2)/(vbusdes/480)-I_Dop;
% tf=demand(end,1);
%% Simulate
opts=simget('mpc_hybrid_sim');
[t,x,y]=sim('mpc_hybrid_sim',[0 tf],opts);
%% Rename Variables
soc_s1=y(:,1)+SOC_op;
ifc_s1=y(:,2)+I_FCop;
iuc_s1=y(:,3);
id_s=y(:,4)+I_Dop;
soc_s2=y(:,5);
diuc_s2=y(:,6);
iuc_s2=y(:,7)+diuc_s2;
ifc_s2=y(:,8);
%% Plot Results
subplot(2,2,1); plot(t,id_s,t,ifc_s1,t,iuc_s1); axis([0 tf -inf inf]);
title('MPC - Current Distribution'); legend('I_D','I_{FC}','I_{UC}');
subplot(2,2,2); plot(t,iuc_s1); title('I_{UC}'); axis([0 tf -inf inf]);
subplot(2,2,3); plot(t,soc_s1); title('SOC'); axis([0 tf -inf inf]);
subplot(2,2,4); plot(t,ifc_s1); title('I_{FC}'); axis([0 tf -inf inf]);
figure
subplot(2,2,1); plot(t,id_s,t,ifc_s2,t,iuc_s2); axis([0 tf -inf inf]);
title('MPC - Current Distribution'); legend('I_D','I_{FC}','I_{UC}');
subplot(2,2,2); plot(t,iuc_s2); title('I_{UC}'); axis([0 tf -inf inf]);
subplot(2,2,3); plot(t,soc_s2); title('SOC'); axis([0 tf -inf inf]);
subplot(2,2,4); plot(t,ifc_s2); title('I_{FC}'); axis([0 tf -inf inf]);
figure
subplot(2,2,1); plot(t,ifc_s1,t,ifc_s2,t,id_s); axis([0 tf -inf inf]);
title('MPC - Current Distribution'); legend('I_{FC}^1','I_{FC}^2','I_D');
subplot(2,2,2); plot(t,iuc_s1,t,iuc_s2);
legend('I_{UC}^1','I_{UC}^2'); axis([0 tf -40 40]);
subplot(2,2,3); plot(t,soc_s1,t,soc_s2);
legend('SOC^1','SOC^2'); axis([0 tf -inf inf]);
subplot(2,2,4); plot(t,ifc_s1,t,ifc_s2);
legend('I_{FC}^1','I_{FC}^2'); axis([0 tf -inf inf]);
%% Save Simulation Data
% clear A1 B1 C1 D1 A2 B2 C2 D2 Cf eta Vmax Vbus x y opts mysys steptime
% clear dt R idemvec pulse_cycle over_discharge over_charge mild_cycle
% clear mix_cycle uc_model tvec inputdelay tau
% clear alpha1 alpha2 beta1 beta2 gamma1 gamma2
% save C:\dSPACE-Experiments\Hybrid_Control\Data_Files\Sim_Data\mpc_080307_test3
```

Figure 4: M-File for Running MPC Controller.

## A.4 MPC Toolbox Compatibility with dSPACE ds1103

As of MATLAB® R2007a, MPC Toolbox™ was not compatible with dSPACE® ds1103 controller board. Errors were generated when compiling any model with an MPC controller containing output constraints. After troubleshooting with Mathworks, it was determined that the compatibility problem was a problem with memory allocation on the ds1103 controller board. The dSPACE® compiler forced MATLAB® to use the 'zalloc' function as opposed to the previously used 'alloc' function.

Patches were provided by Mathworks which are needed on the MPC toolbox™ s-function in order for models incorporating an MPC block to run on dSPACE® ds1103 processor. These patches are only required on releases prior to MATLAB® R2008a and can be retrieved from Mathworks along with documentation describing their use.

# Appendix B MATLAB® Rule-Based Controller Files

## B.1 Rule-Based Control: Simulink Model

Figure 5 shows the Simulink® model used for the real-time implementation of the rule-based controller. The controller was developed using the s-function builder available through Simulink® . An s-function was created which implements the predetermined rules based on feedback from the system. The model was compiled using Real-Time Workshop® to the dSPACE® ds1103 controller board.

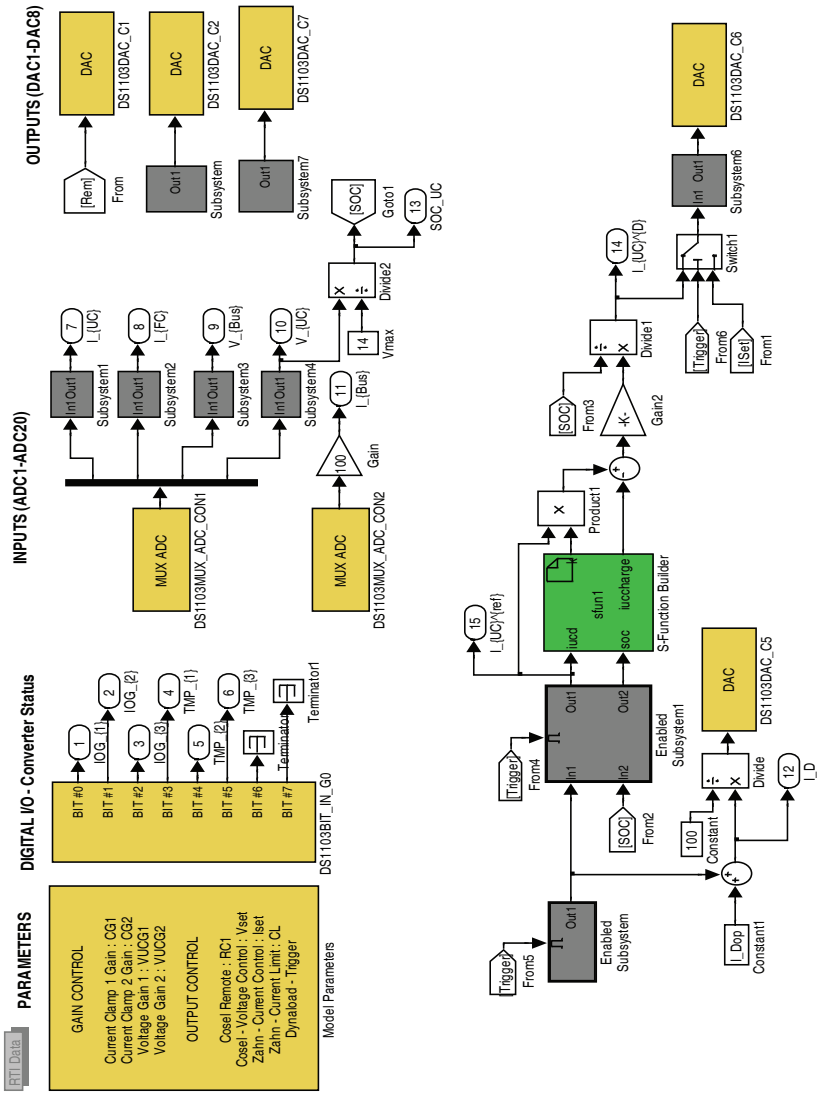


Figure 5: Rule-Based Controller - Simulink® Model.

## B.2 S-function Wrapper

The s-function wrapper that was written to implement the rule-based control action is shown below. Figure 6 contains the first page of the s-function wrapper.



```
/*
  *
  *   --- THIS FILE GENERATED BY S-FUNCTION BUILDER: 3.0 ---
  *
  *   This file is a wrapper S-function produced by the S-Function
  *   Builder which only recognizes certain fields.  Changes made
  *   outside these fields will be lost the next time the block is
  *   used to load, edit, and resave this file. This file will be overwritten
  *   by the S-function Builder block. If you want to edit this file by hand,
  *   you must change it only in the area defined as:
  *
  *        %%%-SFUNWIZ_wrapper_XXXXX_Changes_BEGIN
  *            Your Changes go here
  *        %%%-SFUNWIZ_wrapper_XXXXXX_Changes_END
  *
  *   For better compatibility with the Real-Time Workshop, the
  *   "wrapper" S-function technique is used.  This is discussed
  *   in the Real-Time Workshop User's Manual in the Chapter titled,
  *   "Wrapper S-functions".
  *
  *   Created: Tue Jan 29 08:47:21 2008
  */


/*
 * Include Files
 *
 */
#if defined(MATLAB_MEX_FILE)
#include "tmwtypes.h"
#include "simstruc_types.h"
#else
#include "rtwtypes.h"
#endif
/* %%%-SFUNWIZ_wrapper_includes_Changes_BEGIN --- EDIT HERE TO _END */
#include <math.h>
/* %%%-SFUNWIZ_wrapper_includes_Changes_END --- EDIT HERE TO _BEGIN */
#define u_width 1
#define y_width 1
/*
 * Create external references here.
 *
 */
/* %%%-SFUNWIZ_wrapper_externs_Changes_BEGIN --- EDIT HERE TO _END */
/* extern double func(double a); */
/* %%%-SFUNWIZ_wrapper_externs_Changes_END --- EDIT HERE TO _BEGIN */

/*
 * Output functions
 *
 */
void sfun1_Outputs_wrapper(const real_T *iucd,
```

Figure 6: Rule-Based S-Function Wrapper: Page 1.

Page 2 of the s-function wrapper used to implement rule-based control is given in Fig. 7.



```
                        const real_T *soc,
                        real_T *k,
                        real_T *iuccharge ,
                const real_T  *xD,
                        const real_T  *dt, const int_T  p_width0,
                        const real_T  *chargestep, const int_T  p_width1,
                        const real_T  *ratelimit, const int_T  p_width2,
                        const real_T  *chargecurrent, const int_T  p_width3,
                        const real_T  *chargedelay, const int_T p_width4)
{
/* %%%-SFUNWIZ_wrapper_Outputs_Changes_BEGIN --- EDIT HERE TO _END */
if (iucd[0]>0) {
    if (soc[0]<0.5)
        k[0]=0;
    else if (soc[0]>=0.5 && soc[0]<0.7)
        k[0]=1-(soc[0]-0.7)*(soc[0]-0.7)*25;
    else
        k[0]=1;
}
else if (iucd[0]<0) {
    if (soc[0]>0.9)
        k[0]=0;
    else if (soc[0]<=0.9 && soc[0]>=0.7)
        k[0]=1-(soc[0]-0.7)*(soc[0]-0.7)*25;
    else
        k[0]=1;
}
else {
    k[0]=0;
}

iuccharge[0]=xD[3];
/* %%%-SFUNWIZ_wrapper_Outputs_Changes_END --- EDIT HERE TO _BEGIN */
}

/*
  * Updates function
  *
  */
void sfun1_Update_wrapper(const real_T *iucd,
                        const real_T *soc,
                        const real_T *k,
                        const real_T *iuccharge ,
                        real_T *xD,
                        const real_T  *dt,  const int_T  p_width0,
                        const real_T  *chargestep,  const int_T  p_width1,
                        const real_T  *ratelimit,  const int_T  p_width2,
                        const real_T  *chargecurrent,  const int_T  p_width3,
                         const real_T *chargedelay, const int_T  p_width4)
{
  /* %%%-SFUNWIZ_wrapper_Update_Changes_BEGIN --- EDIT HERE TO _END */
real_T previous,climit,deliucd,cstart;
```

Figure 7: Rule-Based S-Function Wrapper: Page 2.

Page 3 of the s-function wrapper used to implement rule-based control is given in Fig. 8.



```
int_T charge;
cstart=chargedelay[0]/dt[0];
climit=chargestep[0]/dt[0];
previous=xD[0];
deliucd=fabs(iucd[0]-previous)/dt[0];

if (soc[0]<=0.7 && iucd[0]>0 && iucd[0]<=20) {
    if (deliucd<ratelimit[0]) {
        xD[1] += 1;
    } else {
        xD[1]=0;
    }
    if (xD[1]>=cstart) {
        xD[3]=chargecurrent[0]*(1-((xD[2]-climit/2)*(xD[2]-climit/2))/((climit/2)*↙
(climit/2)));
        charge=1;
    } else {
        xD[3]=0;
        charge=0;
    }
} else {
    xD[1]=0;
    xD[2]=0;
    xD[3]=0;
}
if (charge) {
    xD[2] += 1;
    if (xD[2]>=climit) {
        xD[3]=0;
        xD[2]=0;
        xD[1]=0;
    } else {
    }
} else {
    xD[2] = 0;
}

xD[0]=iucd[0];
/* %%%-SFUNWIZ_wrapper_Update_Changes_END --- EDIT HERE TO _BEGIN */
}
```

Figure 8: Rule-Based S-Function Wrapper: Page 3.

## B.3 MATLAB m-file for Loading Controller

The m-file used to set up the rule-based controller Simulink$^{TM}$ model is shown in Fig. 9.

3/25/08 8:29 AM C:\dSPACE-Experiments\Hybrid_Control\Rule_Based\run_rule_based.m 1 of 1

```
%% Run rule_based_hybrid
clear all; close all; clc;
%% System Parameters and Operating Point
Cf=200; Vmax=14; Vbus=24; eta=.85;
I_FCop=20; I_Dop=20; SOC_op=0.7;
%% Rule-Based Control Parameters
dt=0.1;             % Discrete-time step (sec)
ratelimit=1.0;      % I_{UC} rate condition (amps/sec)
chargedelay=3.0;    % Delay time to begin active charging (sec)
chargestep=20.0;    % Active charging duration (sec)
chargecurrent=2.0;  % Max active charging current
%% Simulation Input
tf=200;
steptime=10;
inputdelay=0;
idemvec=[15 10 15 20 25 30 35 30 25 20 15 10 10 15 20 30 10 30 20]-I_Dop;
% idemvec=[10 15 20 25 30 30 25 20 15 10 20]-I_Dop;
tvec=[0:dt:tf]';
%% Load Drive Cycle Data
% steptime=1;
% vbusdes=150;
% load C:\dSPACE-Experiments\Hybrid_Control\Drive_Schedule_Current\IM240
% demand(:,2)=demand(:,2)/(vbusdes/480)-I_Dop;
% tf=demand(end,1);
%% Filters
tau_soc=1;
soc_filt=ss([-1/tau_soc],[1/tau_soc],[1],[0]);
tau_iucd=1/dt;
iucd_filt=ss([-1/tau_iucd],[1/tau_iucd],[1],[0]);
%% Simulate
opts=simget('sim_rule_based_hybrid');
[t,x,y]=sim('sim_rule_based_hybrid',[0 tf],opts);
%% Rename Variables
iuc_s=y(:,1);
soc_s=y(:,2);
isupp=y(:,3);
k=y(:,4);
iucd_s=y(:,5);
id_s=y(:,6)+I_Dop;
ifc_s=id_s-iuc_s;
ifcd_s=id_s-iucd_s;
%% Plot Results
subplot(2,2,1); plot(t,id_s,t,ifc_s,t,iuc_s); axis([0 tf -inf inf]);
title('Rule Based - Current Distribution'); legend('I_D','I_{FC}','I_{UC}');
subplot(2,2,2); plot(t,iuc_s,t,iucd_s); legend('I_{UC}','I_{UC}^D');
title('I_{UC}'); axis([0 tf -inf inf]);
subplot(2,2,3); plot(t,soc_s); title('SOC'); axis([0 tf -inf inf]);
subplot(2,2,4); plot(t,ifc_s); title('I_{FC}'); axis([0 tf -inf inf]);
figure
plot(t,k,t,isupp); legend('k','iucsupp')
```

Figure 9: M-File for Running Rule-Based Controller.

# Appendix C dSPACE® Control Desk

Figure 10 shows Control Desk™ , the user interface between the real-time hardware provided by dSPACE® .

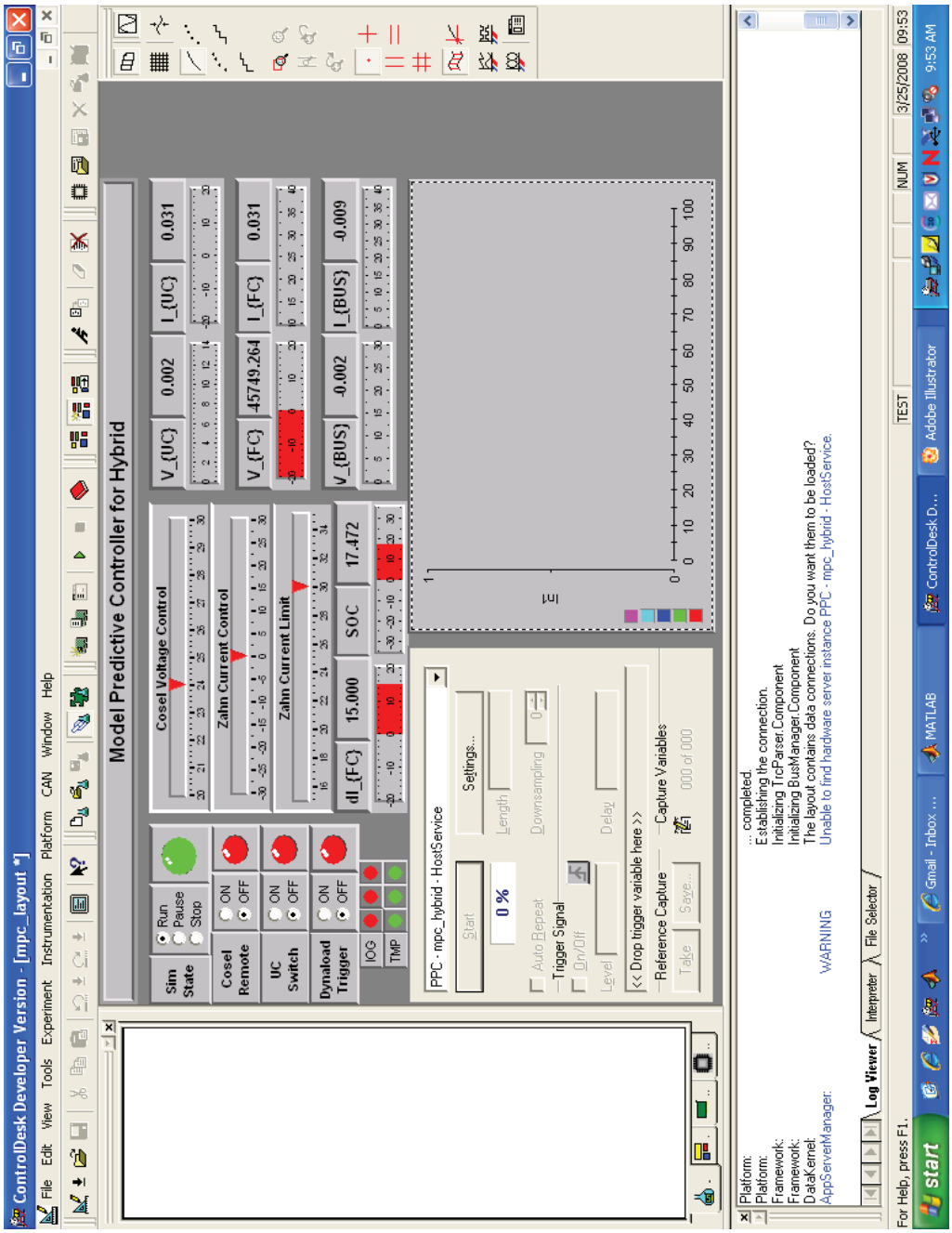


Figure 10: Control Desk User Interface.

# Appendix D Drive Schedules

## D.1 Drive Schedule Model Data

Figure 11 shows six commonly used drive schedules for the testing of automobiles. In order to utilize these standard drive cycles, a simple pitch and heave drive model was used to determine the traction power required to maintain the velocity specified in the profile. The model considered rolling resistance of tires, aerodynamic drag force, and required traction force. The model also considered front and rear aerodynamic down forces and suspension deflections.

After finding the traction power required to maintain vehicle velocity, the problem was simplified by assuming that the motor and drivetrain were 100% efficient. Although this assumption is far from true, it is sufficient for the purposes needed here. Therefore the traction power is the equivalent electrical power needed to maintain velocity. Because this was very large power and our test stand is relatively small, the power was scaled by assuming our bus voltage was $480V$.

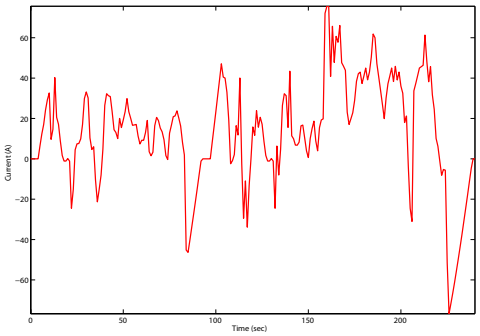


(a) Inspection and Maintenance Drive Schedule

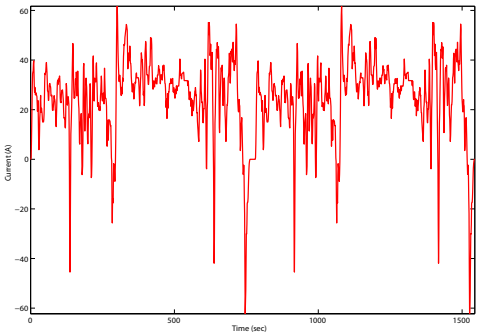


(b) Highway Fuel Economy Drive Schedule

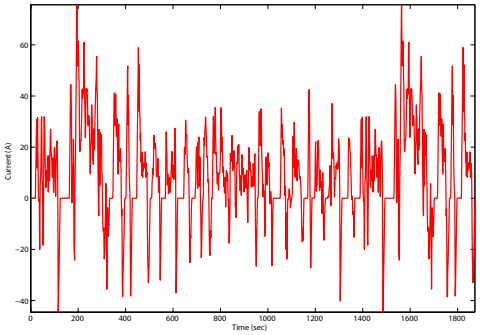


(c) EPA Federal Test Procedure

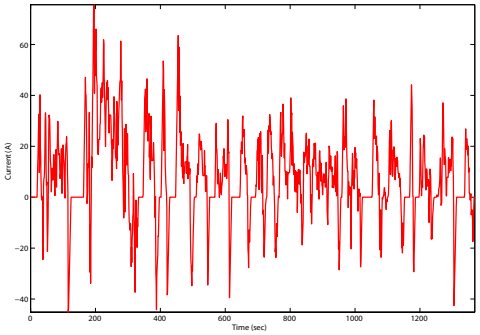


(d) Urban Dynamometer Drive Cycle

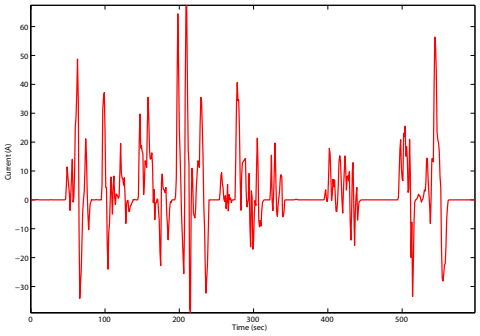


(e) New York City Cycle

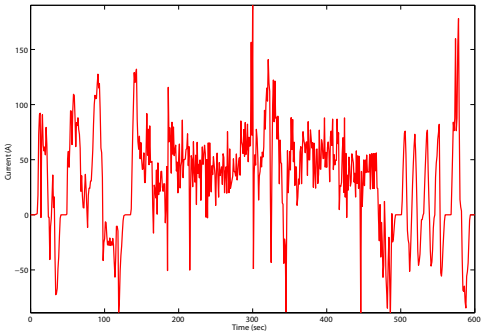


(f) High Acceleration Aggressive Drive Cycle

Figure 11: Drive Schedules Current Profiles

# Appendix E Model Predictive Control

Model predictive control (MPC) is an optimization-based approach for controlling dynamic systems, especially those with hard pointwise-in-time constraints on inputs, states or outputs. A linear state space representation of the system model is used to predict responses to potential control actions, and determines the optimal control actions by minimizing a performance index over a finite horizon. Process constraints on the inputs, outputs, and states can be explicitly enforced in the optimization. MPC is also versatile in that it can control multiple-input multiple-output (MIMO) systems in optimal fashion.

## E.1 General Problem Formulation

Model predictive control is based on the principle of receding horizon optimal control. At each iteration of this fixed-step process, a performance index, or cost function is minimized over a finite prediction horizon of length N. A sequence of M optimal control actions are determined, where M is the control horizon. The first control input of this sequence is applied and the process is repeated. This process of continuously revising the control strategy based on each current system state and moving the optimization window forward in time is the reason for the term "receding horizon" optimal control. The objective function takes the general form shown by Eq. 1.

$$J_N(\{x_k\},\{u_k\}) = \frac{1}{2}x_N^T P x_N + \frac{1}{2}\sum_{k=0}^{N-1}(x_k^T Q x_k + u_k^T R u_k) \tag{1}$$

where $\{u_k\}$ is the control sequence for the specified control horizon $M$, $\{x_k\}$ is the sequence of state variables for the specified prediction horizon $N$, and the two are related by discrete form state space model Eq. 2. The state weighting matrix ($Q$), the control weighting matrix ($R$), and the terminal state weighting matrix ($P$) are used to adjust the performance variables to meet the desired objectives.

$$\begin{aligned} x_{k+1} &= Ax_k + Bu_k \\ y_k &= Cx_k + Du_k \end{aligned} \tag{2}$$

If the system is linear and subject to linear constraints, a quadratic programming (QP) problem can be formulated by recursive use of the discrete time model (Eq. 2) in the cost function from Eq. 1. The standard MPC formulation does not lend itself to the direct injection term $Du_k$; this term is removed by augmenting fast filters to the system as explained in section 2.5.2. Also to ensure zero steady-state error a step disturbance model is augmented with the system. A costant disturbance $d_k$ is estimated at each sample time by comparing

the measured output and predicted output. This constant disturbance is added to future measurements. The effect can be shown to be an integrating influence, ensuring that the actual output tracks a desired reference when feasible. Therefore the output equations will be given by Eq. 3.

$$\begin{aligned} y_k &= Cx_k + d_k \\ d_{k+1} &= d_k \end{aligned} \tag{3}$$

The system under consideration has $n$ state variables, $m$ inputs, and $p$ outputs. The size of the matrices A, B, and C are $\{n \times n\}$,$\{n \times m\}$, and $\{p \times n\}$, respectively.

It is desirable for the system outputs to track a reference trajectory and reject output disturbances. The error between the output and reference trajectories ($y^{ref}$) can be determined from the state output model as shown in Eq. 4. It is desirable to drive this error to zero.

$$e_k = y_k - y^{ref} = Cx_k + d_k - y^{ref} \tag{4}$$

At steady state, the error should be equal to zero ($e_s = 0$), and the output should be equal to the reference ($y_s = y^{ref}$). Using these facts, Eq. 4 can be simplified to give the steady state output as shown in Eq. 5.

$$y_s = y^{ref} = Cx_s + d_s \tag{5}$$

Through further manipulation of the steady state model, the equations for the steady state input and state variables can be derived and are given by Eqs. 6 and 7.

$$u_s = [C(I-A)^{-1}B]^{-1}(y^{ref} - d_s) \tag{6}$$

$$x_s = (I-A)^{-1}Bu_s \tag{7}$$

The disturbance, $d_k$, is assumed constant during the entire prediction horizon and the current state measurement. Our objective is now to find the optimal control sequence, $\{u_0, \ldots, u_{M-1}\}$, the corresponding state variable sequence, $\{x_0, \ldots, x_N\}$, and the error sequence, $\{e_0, \ldots, e_{N-1}\}$ that minimize the following cost

function (8) that is a slight alteration of equation 1.

$$\begin{aligned} J_{N,M}(\{x_k\},\{u_k\},\{e_k\}) = \quad & \tfrac{1}{2}(x_N - x_s)^T P(x_N - x_s) + \tfrac{1}{2}\sum_{k=0}^{N-1} e_k^T Q e_k \\ & + \tfrac{1}{2}\sum_{k=0}^{M-1}(u_k - u_s)^T R(u_k - u_s) \end{aligned} \tag{8}$$

Here $P$,$Q$, and $R$ are the weighting matrices discussed previously. Also note that the the control is set equal to the steady state set-point after M iterations ($u_k = u_s \ \ \forall \ \ k \geq M$). The problem described above is the fixed horizon cost function that should be minimized for each iteration of the method. After the function is minimized, only the first control input, $u_1$, from the control sequence, $\{u_1, \ldots, u_M\}$, should be applied to the plant. The control input is maintained until the next time step, when the entire process is repeated for the new state of the system.

## E.2 MPC Controller Implementation Alterations

As stated previously, model predictive control requires a linear model of the system in order to predict the future system responses to inputs. Nonlinear system models must be linearized around an operating point before the controller can be developed. The standard linearized state space form of the system model is generally written in the form shown in Eq. 9.

$$\begin{aligned} \dot{x} &= [A]x + [B]u \\ y &= [C]x + [D]u \end{aligned} \tag{9}$$

In a standard implementation, MPC cannot handle feedforward (feedthrough) terms in the state-space model. In the MPC Toolbox, any direct feedthrough terms between the manipulated variable and measured outputs creates an error during compilation. In order to avoid this, the feedthrough term is augmented to the state vector. As an example, consider the state-space model with feedforward matrix "D" in Eq. 9.

By defining an approximation of $u$ as $u_f$ through a very fast (small $\tau$) first order filter, the feedthrough term can be augmented to the state variable and the $D$ matrix is eliminated. The fast filter is described by,

$$\frac{u_f(s)}{u(s)} = \frac{1}{\tau s + 1} \qquad \Longrightarrow \qquad \dot{u_f} = \frac{1}{\tau}u - \frac{1}{\tau}u_f \tag{10}$$

By augmenting this relationship in the original state space equation, Eq. 9 can be written as shown

in Eq. 11. As long as $\tau$ is small, $u_f$ is a very accurate approximation for $u$.

$$\begin{aligned} \begin{bmatrix} \dot{x} \\ \dot{u_f} \end{bmatrix} &= \begin{bmatrix} A & B \\ 0 & -\frac{1}{\tau} \end{bmatrix} \begin{bmatrix} x \\ u_f \end{bmatrix} + \begin{bmatrix} 0 \\ \frac{1}{\tau} \end{bmatrix} u \\ y &= \begin{bmatrix} C & D \end{bmatrix} \begin{bmatrix} x \\ u_f \end{bmatrix} \end{aligned} \tag{11}$$

# Bibliography


[1] G. Allen. How An Ultracapacitor Works, September 2007. [Online; accessed 27-February-2008] URL: http://www.ultracapacitors.org/ultracapacitors.org-articles/how-an-ultra-capacitor-works-3.htm.

[2] J. Anstrom, H. Hofmann, B. Zile, K. Smith, and A. Batra. Simulation and Field-Testing of Hybrid Ultra-Capacitor/Battery Energy Storage Systems for Electric and Hybrid-Electric Transit Vehicles. *IEEE Annual Applied Power Electronics Conference and Exposition*, 1:491–497, March 2005.

[3] Ballard Power Systems, Inc. *FC 101: An Introduction to Fuel Cells and Related Technologies*, 2003. http://www.ballard.com.

[4] O. Barbarisi, E. R. Westervelt, F. Vasca, and G. Rizzoni. Power Management Decoupling Control for a Hybrid Electric Vehicle. *IEEE Conference on Decision and Control*, pages 2012–2017, December 2005.

[5] B. M. Baumann, G. Washington, B. C. Glenn, and G. Rizzoni. Mechatronic Design and Control of Hybrid Electric Vehicles. *IEEE/ASME Transactions on Mechatronics*, 5(1):58–72, March 2000.

[6] S. Bontour, D. Hissel, H. Gualous, F. Harel, and J. M. Kauffmann. Design of a Parallel Fuel Cell - Supercapacitor Auxiliary Power Unit (APU). *International Conference on Electrical Machines and Systems*, 2:911–915, September 2005.

[7] B. K. Bose and M. D. Kankam. Power and Energy Storage Devices for Next Generation Hybrid Electric Vehicle. *Energy Conversion Engineering Conference*, 3:1893–1898, August 1996.

[8] A. Brahma, Y. Guezennec, and G. Rizzoni. Optimal Energy Management in Series Hybrid Electric Vehicles. *American Control Conference*, pages 60–64, June 2000.

[9] A. Burke. Ultracapacitors: why, how, and where is the technology. *Journal of Power Sources*, 91(1):37–50, November 2000.

[10] A. Burke. Update of Ultracapacitor Technology for Hybrid Vehicle Applications: Passenger Cars and Transit Buses. *University of California-Davis: Institute of Transportation Studies*, October 2001.

[11] A. Burke. The Present and Projected Performance and Cost of Double-layer and Pseudo-capacitive Ultracapacitors for Hybrid Vehicle Applications. *IEEE Vehicle Power and Propulsion Conference*, pages 356–366, September 2005.

[12] A. Burke. Batteries and Ultracapacitors for Electric, Hybrid, and Fuel Cell Vehicles. *IEEE*, 95(4):806–820, April 2007.

[13] A. Burke and M. Miller. Characteristics of Advanced Carbon-Based Ultracapacitors. *Proceedings of the 10th International Seminar on Double-layer Capacitors and Similar Energy Storage Devices*, 2000.

[14] A. F. Burke. Prospects for Ultracapacitors in Electric and Hybrid Vehicles. *IEEE Battery Conference on Applications and Advances*, pages 183–188, January 1996.

[15] D. Candusso, I. Valero, A. Walter, S. Bacha, E. Rulliere, and B. Raison. Modelling, Control and Simulation of a Fuel Cell Based Power Supply System with Energy Management. *IEEE Annual Conference of the Industrial Electronics Society*, 2:1294–1299, November 2002.

[16] E. Cegnar, H. Hess, and B. Johnson. A Purely Ultracapacitor Energy Storage System for Hybrid Electric Vehicles Utilizing a Microcontroller Based DC-DC Converter. *IEEE Annual Applied Power Electronics Conference and Exposition*, 2:1160–1164, 2004.

[17] W. Choi, J. Howze, and P. Enjeti. Development of an equivalent circuit model of a fuel cell to evaluate the effects of inverter ripple current. *Journal of Power Sources*, 158:1324–1332, November 2006.

[18] B. Conway. Electrochemical capacitors. In *Electrochemistry Encyclopedia*. Electrochemical Science and Technology Information Resource (ESTIR), 1999.

[19] J. M. Correa, F. A. Farret, L. N. Canha, and M. G. Simoes. An Electrochemical-Based Fuel-Cell Model Suitable for Electrical Engineering Automation Approach. *IEEE Transactions on Industrial Electronics*, 51(5):1103–1112, October 2004.

[20] S. Dietz and V. Nguyen. Mesoporous Carbon Electrodes for Double Layer Capacitors. *NSF Design, Service and Manufacturing Grantees and Research Conference*, January 2002.

[21] S. Dietz and D. Recla. Development and Production of Inexpensive Carbons for Double Layer Capacitors. *14th International Seminar on Double Layer Capacitors and Hybrid Energy Storage Devices*, pages 1–7, December 2004.

[22] Rajashekara Emadi. Topological Overview of Hybrid Electric and Fuel Cell Vehicular Power System Architectures and Configurations. *IEEE Transactions on Vehicular Technology*, 54(3):763–770, May 2005.

[23] J. Fenton and R. Hodkinson. *Lightweight Electric/Hybrid Vehicle Design: Automotive Engineering Series*. Elsevier Butterworth-Heinemann, 2000.

[24] A. Ferreira, J. Pomilio, G. Spiazzi, and L. Silva. Energy Management Fuzzy Logic Supervisory for Electric Vehicle Power Supplies. *IEEE Transactions on Power Electronics*, 23(1):107–115, January 2008.

[25] L. Gao, A. Dougal, and S. Liu. Power Enhancement of an Actively Controlled Battery/Ultracapacitor Hybrid. *IEEE Transactions on Power Electronics*, 20(1):236–243, January 2005.

[26] W. Gao. Performance Comparison of a Fuel Cell-Battery Hybrid Powertrain and a Fuel Cell-Ultracapacitor Hybrid Powertrain. *IEEE Transactions on Vehicular Technology*, 54(3):846–855, May 2005.

[27] M. Garcia-Arregui, C. Turpin, and S. Astier. Direct connection between a fuel cell and ultracapacitors. *IEEE International Conference on Clean Electrical Power*, pages 474–479, May 2007.

[28] F. Gassmann, R. Kotz, and A. Wokaun. Supercapacitors Boost the Fuel Cell Car. *Europhysics News*, 34(5), 2003.

[29] Y. Guezennec, T. Choi, G. Paganelli, and G. Rizzoni. Supervisory Control of Fuel Cell Vehicles and its Link to Overall System Efficiency and Low-Level Control Requirements. *American Control Conference*, pages 2055–2061, June 2003.

[30] C. E. Holland, J. W. Weidner, R. A. Dougal, and R. E. White. Experimental characterization of hybrid power systems under pulse current loads. *Journal of Power Sources*, 109:32–37, January 2002.

[31] Y. Jia, H. Wang, and M. Ouyang. Electric Power System for a Chinese Fuel Cell City Bus. *Journal of Power Sources*, 155:319–324, November 2006.

[32] Z. Jiang, L. Gao, M. J. Blackwelder, and R. A. Dougal. Design and experimental tests of control strategies for active hybrid fuel cell/battery power pources. *Journal of Power Sources*, 130:163–171, December 2004.

[33] P. B. Jones, J. B. Lakeman, G. O. Mepsted, and J. M. Moore. A hybrid power source for pulse power applications. *Journal of Power Sources*, 80:242–247, December 1999.

[34] M. Kim and H. Peng. Power management and design optimization of fuel cell/battery hybrid vehicles. *Journal of Power Sources*, 165:819–832, December 2007.

[35] S. Knights, K. Colbow, J. St-Pierre, and D. Wilkinson. Aging mechanisms and lifetime of PEFC and DMFC. *Journal of Power Sources*, 127:127–134, 2004.

[36] W. Lajnef, J. M. Vinassa, O. Briat, S. Azzopardi, and E. Woirgard. Characterization methods and modelling of ultracapacitors for use a peak power sources. *Journal of Power Sources*, 168:553–560, February 2007.

[37] H. Lee, K. Jeong, and B. Oh. An experimental study of controlling strategies and drive forces for hydrogen fuel cell hybrid vehicles. *International Journal of Hydrogen Energy*, 28:215–222, March 2003.

[38] A. W. Leedy and R. M. Nelms. Analysis of a Fuel Cell/Battery-Capacitor Hybrid Sources Used for Pulsed Load Applications. *SAE Transactions - Journal of Aerospace*, pages 825–832, October 2002.

[39] C. Lin, H. Peng, and J. Grizzle. A Stochastic Control Strategy for Hybrid Electric Vehicles. *American Control Conference*, pages 4710–4715, July 2004.

[40] C. Lin, H. Peng, J. Grizzle, and J. Kang. Power Management Strategy for a Parallel Hybrid Electric Truck. *IEEE Transactions on Control Systems Technology*, 11(6):839–849, November 2003.

[41] B. Maher, J. Dogertom, and T. Fisher. Fuel Cells and Ultracapacitors: a Proven Value Proposition versus Incumbent Technologies. *International Telecommunications Energy Conference*, pages 1–4, September 2006.

[42] Maxwell Technologies, Inc. *Energy Datasheet: MC BMOD Energy Series 16v*. [Online; accessed 27-February-2008] URL: http://www.maxwell.com/pdf/uc/datasheets/mc_energy_series_16v_1009362_rev5.pdf.

[43] Maxwell Technologies, Inc. *User Manual: BOOSTCAP Energy Storage Module*, 2005. URL: http://www.maxwell.com.

[44] J. Mierlo, P. Bossche, and G. Maggetto. Models of energy sources for EV and HEV: fuel cells, batteries, ultracapacitors, flywheels, and engine-generators. *Journal of Power Sources*, 128:76–89, September 2004.

[45] J. Moreno, M. Ortuzar, and J. Dixon. Energy Management System for a Hybrid Electric Vehicle, Using Ultracapacitors and Neural Networds. *IEEE Transactions on Industrial Electronics*, 53(2):614–623, April 2006.

[46] C. Musardo, G. Rizzoni, and B. Staccia. A-ECMS: An Adaptive Algorithm for Hybrid Electric Vehicle Energy Management. *44th Annual IEEE Conference on Decision and Control*, pages 1816–1823, December 2005.

[47] Characteristics of Rechargeable Batteries. Application note, National Semiconductor Co. URL: www.national.com/appinfo/power/files/f19.pdf.

[48] Introduction to Power Supplies. Application Note 556, National Semiconductor Co., September 2002. URL: www.national.com/an/AN/AN-556.pdf.

[49] Nesscap Co. Ltd. *Nesscap Ultracapacitor Technical Guide*. [Online; accessed 11-January-2008] URL: http://www.nesscap.com.

[50] NESSCAP Co., Ltd. *NESSCAP Ultracapacitor Products*, 2007. URL: http://www.nesscap.com/data_nesscap/spec_sheets/Spec%2009.pdf.

[51] M. Ortuzar, J. Moreno, and J. Dixon. Ultracapacitor-Based Auxiliary Energy System for an Electric Vehicle: Implementation and Evaluation. *IEEE Transactions on Industrial Electronics*, 54(4):2147–2156, August 2007.

[52] E. Ozatay, B. Zile, J. Anstrom, and S. Brennan. Power Distribution Control Coordinating Ultracapacitors and Batteries for Electric Vehicles. *American Control Conference*, pages 4716–4721, July 2004.

[53] G. Paganelli, M. Tateno, A. Brahma, G. Rizzoni, and Y. Guezennec. Control development for a hybrid-electric sport-utility vehicle: strategy, implementation and field test results. *American Control Conference*, pages 5064–5069, June 2001.

[54] L. V. Perez, G. R. Bossio, D. Moitre, and G. O. Garcia. Optimization of power management in an hybrid electric vehicle using dynamic programming. *Mathematics and Computers in Simulation*, 73:244–254, July 2006.

[55] P. Pisu and G. Rizzoni. A Comparative Study of Supervisory Control Strategies for Hybrid Electric Vehicles. *IEEE Transactions on Control Systems Technology*, 15(3):506–518, May 2007.

[56] K. Rajashekara. Propulsion System Strategies for Fuel Cell Vehicles. *SAE World Congress*, March 2000.

[57] Princeton Applied Research. Fuel cell research, 2004. [Online; accessed 27-February-2008] URL: http://www.princetonappliedresearch.com/products/markets/fuel_cell.cfm.

[58] P. Rodatz, G. Paganelli, A. Sciarretta, and L. Guzzella. Optimal power management of an experimental fuel cell/supercapacitor powered hybrid vehicle. *Control Engineering Practice*, 13:41–53, December 2005.

[59] M. Salman, N. J. Schouten, and N. A. Kheir. Control Strategies for Parallel Hybrid Vehicles. *American Control Conference*, pages 524–528, June 2000.

[60] A. Schell, H. Peng, D. Tran, E. Stamos, C. Lin, and M. Kim. Modelling and Control Strategy Development for Fuel Cell Electric Vehicles. *Annual Reviews in Control*, 29:159–168, February 2005.

[61] M. E. Schenck, J. S. Lai, and K. Stanton. Fuel Cell and Power Conditioning System Interactions. *Applied Power Electronics Conference and Exposition*, 1:114–120, March 2005.

[62] N. Schouten, M. Salman, and N. Kheir. Fuzzy Logic Control for Parallel Hybrid Vehicles. *IEEE Transactions on Control Systems Technology*, 10(3):460–468, May 2002.

[63] A. Sciarretta, M. Back, and L. Guzzella. Optimal Control of Parallel Hybrid Electric Vehicles. *IEEE Transactions on Control Systems Technology*, 12(3):352–363, May 2004.

[64] L. Solero, A. Lidozzi, and J. A. Pomilio. Design of Multiple-Input Power Converter for Hybrid Vehicles. *IEEE Transactions on Power Electronics*, 20(5):1007–1016, September 2005.

[65] J. St-Pierre, D. Wilkinson, S. Knights, and M. Bos. Relationships between water management, contamination and lifetime degradation in PEFC. *Journal of New Materials for Electrochemical Systems*, 3:99–106, 2000.

[66] P. Thounthong, S. Rael, and B. Davat. Control of Fuel Cell/Supercapacitor Hybrid Power Sources. *IEEE Industrial Electronics Society*, pages 768–773, November 2005.

[67] P. Thounthong, S. Rael, and B. Davat. Utilizing Fuel Cell and Supercapacitors for Automotive Hybrid Electrical System. *IEEE Applied Power Electronics Conference and Exposition*, 1:90–96, March 2005.

[68] P. Thounthong, S. Rael, and B. Davat. Control strategy of fuel cell/supercapacitors hybrid power sources for electric vehicle. *Journal of Power Sources*, 158:806–814, September 2006.

[69] P. Thounthong, S. Rael, and B. Davat. Test of a PEM fuel cell with low voltage static converter. *Journal of Power Sources*, 153:145–150, January 2006.

[70] E. Ubong, C. Mizell, G. Slota, and N. Lovria. Ultracapacitor With Ballard Nexa In a GEM Vehicle in a Hybrid Mode. *IEEE Electrical Insulation Conference and Electrical Manufacturing Expo*, pages 317–320, October 2005.

[71] M. Uzunoglu and M. Alam. Dynamic Modeling, Design, and Simulation of a Combined PEM Fuel Cell and Ultracapacitor System for Stand-Alone Residential Applications. *IEEE Transactions on Energy Conversion*, 21(3):767–775, September 2006.

[72] A. Vahidi and W. Greenwell. A Decentralized Model Predictive Control Approach to Power Management of a Fuel Cell-Ultracapacitor Hybrid. *American Control Conference*, pages 5431–5437, July 2007.

[73] A. Vahidi, A. Stefanopoulou, and H. Peng. Current Management in a Hybrid Fuel Cell Power System: A Model-Predictive Control Approach. *IEEE Transactions on Control Systems Technology*, 14(6):1047–1057, November 2006.

[74] J. Webster. Capacitor storage. In *Wiley Encyclopedia of Electrical and Electronics Engineering*. John Wiley and Sons, Inc., Boca Raton, 1999.

[75] Wikipedia. Fuel cell — Wikipedia, The Free Encyclopedia, 2008. [Online; accessed 10-March-2008] URL: http://en.wikipedia.org/w/index.php?title=Fuel_Cell.

[76] Wikipedia. Supercapacitor — Wikipedia, The Free Encyclopedia, 2008. [Online; accessed 27-February-2008] URL: http://en.wikipedia.org/w/index.php?title=Supercapacitor.

[77] Wikipedia. Switched-mode power supply — Wikipedia, The Free Encyclopedia, 2008. [Online; accessed 5-March-2008] URL: http://en.wikipedia.org/w/index.php?title=Switched-mode_power_supply.

[78] X. Yan, A. Seckold, and D. Patterson. Development of a Zero-Voltage-Transistion Bidirectional DC-DC Converter for a Brushless DC Machine EV Propulsion System. *Power Electronics Specialists Conference*, 4:1661–1666, 2002.

[79] G. Zorpette. Super Charged. *IEEE Spectrum*, pages 32–37, January 2005.